Acta Biomaterialia 174 (2024) 281–296

Contents lists available at ScienceDirect

Acta Biomaterialia

journal homepage: www.elsevier.com/locate/actbio

Full length article

Engineering a biomimetic system for hepatocyte-specific RNAi treatment of non-alcoholic fatty liver disease

Xuan He[b,c,1], Zhimin Chang[d,1], Fangman Chen[d,*], Wensheng Zhang[a], Madi Sun[b], Tongfei Shi[b], Jie Liu[a], Peiyu Chen[b], Kunbao Zhang[b], Shan Guan[e], Zhibin Zhao[f], Mingqiang Li[g], Wen-fei Dong[d], Dan Shao[c,f,*], Chao Yang[a,*]

[a] Department of Orthopedics, Guangdong Provincial Key Laboratory of Bone and Joint Degeneration Diseases, The Third Affiliated Hospital of Southern Medical University, Guangzhou 510630, China
[b] School of Biomedical Sciences and Engineering, South China University of Technology, Guangzhou International Campus, Guangzhou 511442, China
[c] National Engineering Research Center for Tissue Restoration and Reconstruction, South China University of Technology, Guangzhou, Guangdong 510006, China
[d] CAS Key Laboratory of Bio Medical Diagnostics, Suzhou Institute of Biomedical Engineering and Technology Chinese Academy of Sciences, Suzhou 215163, China
[e] National Engineering Research Center of Immunological Products, The Third Military Medical University, Chongqing 400038, China
[f] School of Medicine, South China University of Technology, Guangzhou, Guangdong 510006, China
[g] Laboratory of Biomaterials and Translational Medicine, Center for Nanomedicine, The Third Affiliated Hospital, Sun Yat-sen University, Guangzhou 510630, China

ARTICLE INFO

Article history:
Received 20 July 2023
Revised 10 October 2023
Accepted 29 October 2023
Available online 10 November 2023

Keywords:
Biomimetic
Hepatocyte-specific
Cell membrane
GalNAc
PCSK9

ABSTRACT

RNA interference (RNAi) presents great potential against intractable liver diseases. However, the establishment of specific, efficient, and safe delivery systems targeting hepatocytes remains a great challenge. Herein, we described a promising hepatocytes-targeting system through integrating triantennary *N*-acetylgalactosamine (GalNAc)-engineered cell membrane with biodegradable mesoporous silica nanoparticles, which efficiently and safely delivered siRNA to hepatocytes and silenced the target PCSK9 gene expression for the treatment of non-alcoholic fatty liver disease. Having optimized the GalNAc-engineering strategy, insertion orders, and cell membrane source, we obtained the best-performing GalNAc-formulations allowing strong hepatocyte-specific internalization with reduced Kupffer cell capture, resulting in robust gene silencing and less hepatotoxicity when compared with cationic lipid-based GalNAc-formulations. Consequently, a durable reduction of lipid accumulation and damage was achieved by systemic administering siRNAs targeting PCSK9 in high-fat diet-fed mice, accompanied by displaying desirable safety profiles. Taken together, this GalNAc-engineering biomimetics represented versatile, efficient, and safe carriers for the development of hepatocyte-specific gene therapeutics, and prevention of metabolic diseases.

Statement of Significance

Compared to MSN@LP-GN3 (MC3-LNP), MSN@CM-GN3 exhibited strong hepatocyte targeting and Kupffer cell escaping, as well as good biocompatibility for safe and efficient siRNA delivery. Furthermore, siPCSK9 delivered by MSN@CM-GN3 reduced both serum and liver LDL-C, TG, TC levels and lipid droplets in HFD-induced mice, resulting in better performance than MSN/siPCSK9@LP-GN3 in terms of lipid-lowering effect and safety profiles. These findings indicated promising advantages of our biomimetic GN3-based systems for hepatocyte-specific gene delivery in chronic liver diseases. Our work addressed the challenges associated with the lower targeting efficiency of cell membrane-mimetic drug delivery systems and the immunogenicity of traditional GalNAc delivery systems. In conclusion, this study provided an effective and versatile approach for efficient and safe gene editing using ligand-integrated biomimetic nanoplatforms.

* Corresponding authors.
E-mail addresses: chenfangman@hotmail.com (F. Chen), stanauagate@outlook.com (D. Shao), charisyang910@gmail.com (C. Yang).
[1] These authors contributed equally to this work.

https://doi.org/10.1016/j.actbio.2023.10.038
1742-7061/

1. Introduction

Chronic liver diseases, particularly viral hepatitis and non-alcoholic fatty liver disease (NAFLD) account for more than 3.5% of global mortality [1,2], due to the lack of curative treatment options. The recent FDA approval of the first siRNA-based therapeutic targeting hereditary transthyretin-mediated amyloidosis underscores RNA interference (RNAi) as a potent strategy for addressing diverse intractable liver diseases by specifically silencing disease-causing genes [3–5]. To harness the therapeutic potential of RNAi-based drugs in the liver, numerous delivery systems have been developed to address three crucial challenges: RNA protection [6], targeted delivery to specific liver cells, and effective release into the cytosol [7–9]. To overcome the obstacle, numerous delivery systems have been developed, including polymer, exosomes, cationic lipids, etc. [10–12].

Among these systems, cationic lipid nanoparticles (LNPs) have gained prominence in clinical settings due to their structural flexibility, scalability in manufacturing, excellent biodegradability, and efficient cytosolic release [13,14]. However, after systematic delivery, RNA-loaded LNPs primarily and rapidly accumulated in the liver [15]. Nevertheless, their broad uptake by liver-specific macrophages (Kupffer cells, KCs) hampers specific hepatocytes targeting [16,17], while their susceptibility to blood instability and hepatoxicity pose major concerns for long-term application [18]. Consequently, effective and safe RNAi delivery systems that are specific and efficient remain a significant obstacle in translating therapies for chronic liver diseases [19,20].

Hepatocytes (HCs) are the main functional units of the liver and are integral to maintaining metabolic homeostasis, which represents a potential target for RNAi modalities [21,22]. Given that the asialoglycoprotein receptor (ASGPR) is specifically and abundantly expressed on hepatocytes, its ligand *N*-acetylgalactosamine (GalNAc) is considered a robust targeting ligand to enable the development of effective and selective RNA delivery systems for hepatocytes [20]. The success of GalNAc-siRNA conjugates in clinical trials has provided a treasure trove for the potent and long-lasting outcomes of RNAi therapy [23]. Inspired by these pioneering examples, several GalNAc-functionalized nanoplatforms have been developed for hepatocyte-specific gene delivery in a versatile, powerful, and long-lasting manner. Nevertheless, the rational design of ASGPR-targeting nanocarriers with low immunogenicity and high HCs/KCs uptake ratio to achieve efficient and safe RNAi therapeutics remains a great challenge.

To address these issues, cell membrane-based nanotherapeutics have emerged as a fruitful approach to improve drug delivery via integrating the functional versatility of nanoplatforms with the biomimetic features of cell membranes [24]. Such facile functionalization is characterized by “coating” drug-encapsulating nanocores with lipid-like membrane layers, which surmounts challenges associated with poor stability and immunogenicity [25,26]. Tailored engineering of the cell membrane using physical, chemical, and genetic approaches offers a wide array of functions, such as prolonged circulation and intrinsic bioactivities [24]. Based on these findings, we believe that integrating the cell membrane layer with GalNAc will facilitate the cell-selectivity of biomimetic nanoplatforms, leading to maximal hepatocyte-specific RNA delivery efficiency and minimizing non-specific scavenging by the reticuloendothelial system (RES). However, it remains unclear whether the interaction between cell membrane vesicles and GalNAc molecules affects HC-specific targeting.

Herein, we introduced a biomimetic approach, CM-GN3, which combines GalNAc-engineering cell membranes with siRNA-loaded biodegradable mesoporous silica nanoparticles (MSNs). We systematically investigated how the HC-targeting efficiency can be modulated through the GalNAc-engineering strategy (covalent or non-covalent method), insertion orders, and cell membrane sources (macrophage or mesenchymal stem cells). After optimizing the best-performing CM-GN3 and illustrating their cellular internalization mechanism, we compared the HC-targeting, KCs-escaping, and gene therapy properties between MSN@CM-GN3 and GalNAc-engineering lipid-coating nanoplatform (MSN@LNP-GN3) *in vitro* and *in vivo*. Ultimately, we demonstrated the therapeutic and safety potential of this biomimetic siRNA delivery system in a high-fat diet-induced NAFLD mouse model targeting proprotein convertase subtilisin *kexin* type 9 (PCSK9) gene. This study provided a proof-of-concept for using a versatile GalNAc-engineering biomimetic approach for efficient and safe hepatocyte-specific siRNA delivery.

2. Materials and methods

2.1. Materials

Tetraethyl orthosilicate (TEOS), 3-aminopropyltriethoxysilane (APTES), bis[3-(triethoxysilyl)propyl]tetrasulfide (BTESPT), etyltrimethylammonium tosylate (CTAT), γ-chloropropyl trimethoxysilane (CP), triethanolamine (TEA), triethanolamine ($TEAH_3$), succinic anhydride and fluorescein isothiocyanate (FITC) were purchased from Sigma-Aldrich Co. (USA). Selenium (Se) powder and ammonium nitrate (NH_4NO_3) were purchased from Beijing Chemical Reagent Co. (China). 4′,6-diamidino-2-phenylindole (DAPI) was purchased from Invitrogen Co. (USA). TNF-α(mouse) ELISA Kit was bought from Elabscience (China). DBCO-PEG200-FITC, DSPE-PEG200-FITC, DBCO-PEG2000-SH, and DSPE-PEG2000-SH were purchased from Kaixin Co. (China). Cy5-labeled siRNA was purchased from Biosyntech Co. (China). PCSK9 ELISA kit was purchased from Spbio Co. (China). TC and TG assay kits were purchased from the Jiancheng bioengineering Institute (China).

2.2. Cell engineering

Both the click reactivity and lipid insertion of the FITC-modified cell membrane were characterized. To achieve this, azide-modified cells or non-modified cells were obtained by culturing them with or without 100 μM Ac_4ManNAz in a complete medium for 72 h and seeded in a confocal microscope dish. Subsequently, DBCO-PEG2000-FITC and DSPE-PEG2000-FITC were respectively added at a final concentration of 100 μM and incubated for 1 h at 37 °C. The cells were washed with cold PBS three times and then stained with DAPI for 15 min. Imaging was carried out using confocal laser scanning microscopy.

2.3. Synthesis of cell engineering ligands

The synthesis of Triantennary *N*-acetylgalactosamine maleimide (Tris-GalNAc) was carried out using a modified protocol as in previous reports [27,28]. To prepare the GN3 ligand, a mixture of DSPE-PEG2000-SH, DBCO-PEG2000-SH, or FITC-SH, and triantennary *N*-acetylgalactosamine maleimide (GN3-maleimide) at a mole ratio of 1:1.2 was prepared in anhydrous dimethyl sulfoxide (DMSO) under nitrogen protection. The thiol-maleimide “click” reactions were carried out in the dark for 48 h at room temperature, and reactions were monitored by thin-layer chromatography. The reaction mixtures were collected, dialyzed, and lyophilized. Bruker Ascend 400 spectrometer was used to detect ^{1}H NMR spectra. MSN-GN3 was also synthesized via thiol-maleinide “click chemistry” reaction using MSN-SH and GN3-maleinide.

2.4. Preparation of biomimetic NPs

RAW264.7 cells were cultured with or without 100 μM Ac_4ManNAz in a complete medium for 72 h to obtain azide-modified cells or cells. Subsequently, the cells were lysed and sonicated on ice using a Vibra-cell VCX 400 probe sonicator with a CV 26 probe (tip diameter of 3 mm). The sonication at 100 W was continuous for 2 min with a working frequency of 30 kHz and durations of 10 sec each. Then, the azide-modified or blank cell membrane fractions were collected by ultracentrifugation. The BCA protein assay kits were employed to measure the total membrane protein concentration. Diselenide-bridged MSNs were prepared according to our previous reports [29,30]. The cell membrane fractions and MSNs were mixed, pipetted, and sonicated to form MSN@CM or MSNs@CM-GN3.

For the fabrication of MSN@CM-GN3-L, DSPE-PEG2000-GN3 was incorporated into the cell membrane vesicles via lipid insertion for 1 h at 37 °C and sonicated for 2 min in an ultrasonic cell disruptor at 100 W. The mole ratio of the GN3 ligand was the same as that used in CM-GN3-C fabricated by click chemistry. The GN3-functionalized cell membrane vesicles were then resuspended to coat mesoporous silica nanoparticles (MSNs) at a ratio of 2:1 (membrane protein: MSN) to form MSN@CM-GN3-L. To prepare MSN@CM-GN3-C by click chemistry, the azide-modified cell membrane was incubated with DBCO-PEG2000-GN3 for 1 h at 37 °C and sonicated for 2 min in an ultrasonic cell disruptor at 100 W. The mass ratio of membrane protein and ligand was 1/2. The GN3-functionalized cell membrane vesicles were sonicated and resuspended to coat MSNs at a mass ratio of 2:1 (membrane protein: MSN) to form MSN@CM-GN3-C.

To investigate the HC-targeting efficiency of insertion orders, MSN@CM-GN3 was prepared by insertion methods I or II. For the preparation of MSN@CM-GN3 by lipid insertion I, MSN, and cell membrane fractions were mixed at an equivalent volume, followed by DSPE-PEG2000-GN3 insertion into the cell membrane, resulting in the formation of MSN@CM-GN3-I. To prepare MSN@CM-GN3 by lipid insertion II, cell membrane fractions, and DSPE-PEG2000-GN3 were applied to fabricate the blank CM-GN3 using sonication for 2 min in an ultrasonic bath sonicator at 100 W. MSNs were mixed with blank CM-GN3 by sonication for 2 min in an ultrasonic bath sonicator at 100 W to form MSN@CM-GN3-II.

The selection of cell membrane sources may impact the efficiency of HC targeting [31]. To investigate this, cell membrane vesicles from RAW264.7 macrophages and bone marrow mesenchymal stem cells (BMSC) were collected by ultracentrifugation following lysis and homogenization. Equivalent masses of membrane vesicles from RAW264.7 and BMSCs were used to prepare GN3-functionalized cell membrane vesicles through lipid insertion with DSPE-PEG2000-GN3 at 37 °C for 1 h, followed by sonication for 2 min in an ultrasonic bath sonicator at 100 W. These vesicles were used to coat MSNs at a mass ratio of 1:2 (MSN: membrane protein) to obtain MSN@CM-GN3-R and MSN@CM-GN3-B, respectively.

2.5. Characterization of NPs

To quantify ligand incorporation onto nanoformulations, different amounts of DSPE-PEG2000-FITC and DBCO-PEG2000-FITC were incubated with nanoformulations for 30 min. The nanoformulations were purified and resuspended to characterize the modification efficiency. The ligand density could be estimated based on its molecular weight and membrane concentration. The physicochemical properties of various nanoformulations were examined to determine their stability and efficacy. Dynamic light scattering was used to measure the size, polydispersity index (PDI), and zeta potential of the cell membrane, MSN, MSN@CM, and MSN@CM-GN3. To assess the stability, MSN@CM-GN3 was suspended in phosphate-buffered saline (PBS) or fetal bovine serum (FBS) and analyzed by DLS. Samples were prepared on a carbon-coated copper grid. The membrane layer on the surface of MSN@CM was visualized using transmission electron microscopy. For SDS-PAGE protein analysis, samples of cells, cell membrane fractions, MSN@CM, MSN@CM-GN3, and MSN were individually prepared in SDS loading buffer at equivalent protein concentrations and loaded into a 10% SDS-gel for PAGE. Positively charged amine-modified MSNs were synthesized and combined with negatively charged siRNA to fabricate MSN/siRNA at an equivalent volume (w:w, 50:1). MSN/siRNA@CM-GN3 and MSN/siRNA@LP-GN3 were prepared by mixing MSN/siRNA with CM-GN3 or LP-GN3 at equivalent volumes. The characterization of MSN/siRNA and MSN/siRNA@CM-GN3 was carried out by DLS and TEM analysis. Encapsulation efficiency and loading capacity were calculated using the following formula.

$$\text{Encapsulation efficiency}(\%) = \frac{\left[\text{m}(\text{total siRNA}) - \text{m}(\text{free siRNA})\right]}{\text{m}(\text{total siRNA})} \times 100\%$$

$$\text{Loading capacity }(\%) = \frac{\left[\text{m}(\text{total siRNA}) - \text{m}(\text{free siRNA})\right]}{\text{m}(\text{total siRNA}) + \text{m}(\text{MSN})} \times 100\%$$

2.6. Cytotoxicity assay and cellular uptake

To evaluate the cytotoxicity of various nanocarriers, including MSN, MSN@CM, MSN@CM-GN3, and MSN@LP-GN3, these particles were dispersed into a complete DMEM medium at a range of concentrations and individually incubated with RAW264.7 cells, L929 cells, and HUVECs in the proper density for 24 h. Then the cell viability was analyzed by SRB assay.

To further assess the efficacy of these nanocarriers in targeting the human hepatocellular liver carcinoma cell line (HepG2), the cells were cultured in DMEM medium at a density of 2×10^5 cells/well. HepG2 cells were initially cultured with or without 100 μg/mL GN3 solution as an inhibitor of ASGPR for 1 h, followed by incubation with MSN, MSN@CM, MSN@CM-GN3-C, and MSN@CM-GN3-L in the medium at 200 μg/mL concentration of MSN for 2 h. The cells were collected, washed, and resuspended in PBS, and the resulting cell suspension was analyzed by BD FACS Celesta and Accuri C6 plus flow cytometer.

For the investigation of lipid insertion orders on HC-targeting efficiency, HepG2 cells were cultured with MSN@CM-GN3-I and MSN@CM-GN3-II at 50 μg/mL concentration of MSN for 4 h at 37 °C. After washing with cold PBS, cellular uptake of MSN@CM-GN3 by different lipid insertion methods was analyzed using flow cytometry.

To determine the cellular internalization of MSN@CM-GN3 at different sources of the cell membrane, RAW264.7 and BMSC cell membrane fractions were sonicated with DSPE-PEG2000-GN3 and used to coat the surface of MSNs. The cells were then cultured with MSN@CM-GN3-R and MSN@CM-GN3-B for 4 h. The resulting cells were washed, collected, and resuspended in PBS for flow cytometry. The cellular uptake of MSN, MSN@CM, MSN@CM-GN3, and MSN@LP-GN3 was assessed in Hepatocytes and Kupffer cells using HepG2 cells and RAW264.7 cells. Cells were incubated for 2 h with or without incubation of GN3 in advance.

Cultured cells were subjected to exposure to particles of varying concentrations and incubated for different periods. Additionally, HepG2 cells were seeded and treated with MSN@CM-GN3 in low, medium, and high GN3 density. The mean fluorescence intensity was subsequently determined via FlowJo software. To evaluate ASGPR expression levels on cell membrane surfaces, HepG2 cells, Hepa1-6 cells, and RAW264.7 cells were stained with FITC-GN3. Finally, quantification of cellular uptake of MSN, MSN@CM,

and MSN@CM-GN3 was achieved using flow cytometry. To compare the cellular uptake of MSN-GN3 and MSN@CM-GN3, HepG2 and RAW264.7 cells were incubated with nanocarriers for 4 h. The fluorescence intensity of nanocarriers was determined.

Cy5-labeled siRNA was encapsulated into MSN@CM-GN3 or MSN@LP-GN3. HepG2 cells were incubated with MSN/Cy5-siRNA, MSN/Cy5-siRNA@CM, and MSN/Cy5-siRNA@CM-GN3 for 4 h, and the resulting cellular uptake efficiency and mean fluorescence intensity were determined using flow cytometry (Beijing Challen Biotechnology Co., Ltd, FongCyte).

2.7. Determining endocytic pathways

HepG2 cells were subjected to incubation with various nanoformulations including MSN, MSN@CM, and MSN@CM-GN3 at different temperatures for 2 h. The resulting cells were washed with cold PBS and the mean fluorescence intensity was determined via flow cytometry. To identify the cellular uptake pathways of various particles, HepG2 cells were first pre-cultured with specific inhibitors for 1 h at 37 °C for different pathways. Chlorpromazine (20 μg/mL) was used to inhibit the clathrin-mediated endocytosis pathway, while nystatin (15 μg/mL) was used to block caveolae-mediated endocytosis. Amiloride (133 μg/mL) was used to prevent micropinocytosis, while sodium azide (1 mg/mL) was used to inhibit cell energy generation. Subsequently, MSN, MSN@CM, MSN@CM-GN3, and MSN@LP-GN3 were diluted in the medium for 2 h at 37 °C. The solution was removed and the cells were washed with cold PBS twice, collected, and resuspended in PBS for analysis via flow cytometry. A comparison of the cellular uptake percentage of particles with inhibitors relative to those without inhibitors was used to infer the specific endocytosis pathways of MSN, MSN@CM, and MSN@CM-GN3.

2.8. In vivo targeting and cell-specific accumulation in the liver

All animal experiments were approved by the Ethics Committee and Institutional Animal Care and Use Committee of the South China University of Technology (Guangzhou, China). Five-week-old male C57BL/6 mice were obtained from Human SJA Laboratory Animal Co., LTD. The mice were divided randomly into three groups and the *in vivo* liver distribution of MSN-ICG, MSN-ICG@CM, and MSN-ICG@CM-GN3 (5 mg/kg) were investigated through intravenous injection by *in vivo* imaging. The ICG fluorescence signals were detected at specified time points using the AniView100 *in vivo* imaging system. Subsequently, the animals were euthanized and various tissues such as the liver, spleen, heart, lung, and kidney were isolated after 2 h and examined using the AniView100 *in vivo* imaging system. The mean fluorescence intensity was quantified using ImageJ software.

C57BL/6 mice were divided randomly into six groups. The groups received intravenous injections of PBS, FITC-MSN, FITC-MSN@CM, FITC-MSN@CM-GN3, GN3+FITC-MSN@CM-GN3, and FITC-MSN@LP-GN3 at a dose of 10 mg/kg, with PBS serving as the control. After 3 h, all animals were anesthetized, and the liver was perfused with EGTA to remove circulating cells and was perfused with collagenase to digest collagen. The cells were then released into suspension and separated into HCs and KCs using percoll with different densities. The fluorescence intensity of different particles in HCs and KCs was measured using a BD FACS Celesta flow cytometer. Furthermore, PBS, Ru-MSN, Ru-MSN@CM, Ru-MSN@CM-GN3, GN3+Ru-MSN@CM-GN3, and Ru-MSN@LP-GN3 were administered via tail vein injection at a dose of 20 mg/kg, and the amount of Ru is quantified was quantified using ICP-MS after isolation of HCs and KCs at 3 h post-injection.

2.9. In vitro and in vivo gene silencing

HepG2 cells were seeded into a 12-well plate at 2×10^5 cells per well. After 24 h, siRNA, MSN/siRNA@CM-GN3, and MSN/siRNA@LP-GN3 were added into wells for siRNA at different concentrations for 12 h or at a final concentration of 100 nM for different time points. The cells were also incubated with MSN@CM-GN3 in different ratios of siRNA and MSN. After incubation, the cells were washed with cold PBS and harvested using the Trizol reagent. RNA was extracted by adding chloroform, centrifuging the samples, adding isopropanol, washing with 75% ethanol, and drying the sediment. The RNA was then reverse-transcribed into DNA and gene silencing was assessed by real-time quantitative polymerase chain reaction (RT-qPCR).

C57BL/6 mice were administered with siRNA, MSN/siRNA@CM-GN3, and MSN/siRNA@LP-GN3 via the tail vein injection at a dose of 0.4 mg/kg. Additionally, siRNA and MSN/siRNA@CM-GN3 were also administered via tail vein at doses of 0.1, 0.2, and 0.4 mg/kg. At predetermined time intervals, all mice were anesthetized, and the blood and liver tissue samples were collected. The liver tissue samples were subsequently preserved in the Trizol reagent for further mRNA expression analysis.

2.10. Lipid-lowing effects of MSN/siRNA@CM-GN3 in HFD-induced model

To establish an HFD-induced NAFLD model, thirty C57BL/6 mice were fed a high-fat diet (60% kcal) from days -98 to -1 with an additional four mice fed a standard chow diet serving as a control [32]. On days 0, 7, and 14, HFD-fed animals were divided into five groups and treated with PBS, MSN, siRNA, MSN/siRNA@CM-GN,3 and MSN/siRNA@LP-GN3, each at an equivalent 0.4 mg/kg siRNA or 20 mg/kg MSN. MSN and siRNA were employed as negative controls. On day 16, all animals were anesthetized and serum was collected. The liver tissues were isolated and then imaged. Adipose tissues, liver, spleen, heart, lung, and kidneys were isolated and fixed in 4% formalin for hematoxylin and eosin (H&E) staining, while necrosis of the liver and adipocyte diameter was calculated using ImageJ software. Furthermore, the NAFLD activity score was assessed by summing the scores of steatosis, inflammation, and ballooning. The liver samples were also stained with oil red O to determine the level of lipid accumulation. Levels of aspartic transaminase (AST), alanine transaminase (ALT), total triglycerides (TG), total cholesterol (TC), low-density lipoprotein cholesterol (LDL-C), high-density lipoprotein cholesterol (HDL-C) were detected using serum biochemistry analysis. Additionally, the relative mRNA expression of PCSK9 and low-density lipoprotein receptor (LDLR) was determined using RT-qPCR. Control animals were fed a standard chow diet and HFD-induced animals were fed a high-fat diet during the whole study.

The levels of PCSK9 in the serum and supernatant of liver tissue suspension were measured using a mouse PCSK9 ELISA Kit. Briefly, the samples were diluted and then incubated in pre-coated plates for 1 h. Following incubation, the wells were washed four times with washing buffer, and an enzyme-labeled antibody was added and incubated for 30 min. Subsequently, the wells were washed four times, and TMB solution was added to each well for a 15-min incubation period in the dark. The stop solution was then added, and the absorbance was measured at 450 nm using a microplate reader. TC and TG levels in both the serum and liver tissues supernatant were assayed using a total cholesterol assay kit and triglyceride assay kit. Moreover, the levels of TNF-α in the serum and liver tissues were analyzed using a mouse TNF-α ELISA kit.

2.11. Statistical analysis

The FlowJo software was employed to analyze the flow cytometry data, while the GraphPad Prism software was utilized for the statistical analysis. The data were undergone one-way or two-way analysis of variance (ANOVA), with a Tukey correction applied. Insignificance was denoted as "ns", whereas P-values less than or equal to 0.05, 0.01, and 0.001 were labeled with *, **, and ***, respectively. The mean values with their corresponding standard error of the mean (SEM) were depicted by each bar.

3. Results

3.1. Preparation and optimization of MSN@CM-GN3

Optimization of the fabrication conditions for MSN@CM-GN3 required adjustments to the engineering GalNAc-functionalized cell membrane layer and camouflage encapsulation of the nanoparticulate core. To this end, we modified the GalNAc-engineering strategy, insertion orders, and cell membrane source. Since physical and chemical engineering were the main methods to fabricate ligand-functionalized nanoparticles, we first investigated the engineering efficiency of the non-covalent and covalent methods. For physical engineering, the cell membrane (CM) was directly fused with DSPE-PEG2000-ligand using a non-covalent method (Fig. 1a). For chemical engineering, the azide-modified cell membrane (CM-N3) was conjugated with DBCO-PEG2000-ligand using covalent method (Fig. 1b). To optimize the coating conditions, FITC-labeled DSPE-PEG2000 or DBCO-PEG2000 were employed to prepare engineered CMs and coated on diselenide-bridged mesoporous silica nanoparticles (MSNs) to form MSN@CM-FITC-L (lipid insertion) and MSN@CM-FITC-C (click chemistry), respectively. The intracellular fluorescence of MSN@CM-FITC-L and MSN@CM-FITC-C were determined using flow cytometry. The fluorescence of cells engineered by using lipid insertion and click chemistry was determined via confocal laser scanning microscopy (Fig. S1). The results revealed that increasing the ligand concentration led to a concentration-dependent manner of engineering ligand-functionalized cell membrane, as evidenced by the increased fluorescence of MSN@CM-FITC-L and MSN@CM-FITC-C with increasing ligand concentrations (Fig. 1c and d). The coating efficacy of the cell membrane-coated MSNs was detected. The NP-to-membrane mass ratio was approximately saturation at 1:2 (Fig. S2). The size and zeta potential of MSN@CM-GN3-L and MSN@CM-GN3-C were evaluated. The results showed that the changes of size and zeta potential exhibited no significance (Fig. S2), indicating that the different method has little impact on particle size and surface charge. Next, the density of GN3 ligand on the surface of the formulation was determined. The MSN@CM-GN3-L and MSN@CM-GN3-C contained approximately 46025 and 8430 GN3s, respectively. These findings indicate that the physical conjugation exhibited better performance of engineering efficiency than that of chemical methods. Specially, physical insertion is done in one step, while chemical modification goes through a complex glycosylation process.

After investigating the engineering efficiency of both physical and chemical methods, we identified optimized conditions for each engineering method. We synthesized DSPE-PEG-GN3 and DBCO-PEG-GN3, utilizing Tris-GalNAc (GN3) with the highest ASGPR binding affinity (Scheme S1 and 2, Fig. S3 and 4). Subsequently, we examined how the physical and chemical engineering of GalNAc affect the hepatocyte-targeting effects of MSN@CM-GN3. The cellular internalization of MSN@CM-GN3-C or MSN@CM-GN3-L was determined by calculating the mean fluorescence intensity through flow cytometry. The results indicated that the cellular uptake of MSN@CM-GN3-L and MSN@CM-GN3-C was significantly increased in comparison to bare MSN or MSN@CM without GN3-engineering (Fig. 1e and f). Moreover, the pre-treatment of GN3 remarkedly reduced the improved internalization of GN3-engineered MSN@CM, indicating that the cellular internalization of MSN@CM-GN3 in hepatocytes may be mediated by ASGPR. Importantly, the hepatocyte targeting of MSN@CM-GN3-L was higher than MSN@CM-GN3-C with the same molecular weight of GN3 ligand and membrane concentration. Consequently, we opted for the non-covalent method to fabricate MSN@CM-GN3 through lipid insertion for further study.

As the sequence of lipid insertion and membrane coating is critical for achieving targeting efficiency [33], we investigated two insertion orders for MSN@CM-GN3-L (lipid insertion I for membrane coating first with lipid insertion second, and lipid insertion II for lipid insertion first with membrane coating second) (Fig. 2a and b). The density of GN3 ligand on the surface of the formulation was determined. The MSN@CM-GN3-L and MSN@CM-GN3-C contained approximately 3427 and 45413 GN3s, respectively, indicating that the lipid insertion II exhibited better performance of engineering efficiency than that of lipid insertion I. The results showed that the cellular uptake of MSN@CM-GN3 fabricated by lipid insertion I did not significantly increase compared to MSN@CM without GN3-engineering (Fig. 2c). In contrast, the cellular uptake of MSN@CM-GN3 fabricated by lipid insertion II showed a significant increase compared to MSN@CM (Fig. 2d). Therefore, we believed that the better hepatocyte-targeting efficiency was achieved by MSN@CM-GN3 fabricated by lipid insertion II, where cell membrane vesicles first inserted with GN3 before coating on the surface of MSN. To further maximize the hepatocyte-targeting efficiency of biomimetic nanoparticles, different sources of cell membranes were investigated. RAW264.7 macrophages and BMSC cell membranes were selected to prepare MSN@CM-GN3. The results showed that the cellular uptake of MSN@CM-GN3-R, fabricated using RAW264.7-derived membrane, was significantly higher than that of MSN@CM-GN3-B, prepared using BMSC-derived membrane (Fig. S5). Based on these findings, we selected MSN@CM-GN3 prepared by inserting GN3 into RAW264.7-derived membrane and coated MSN for subsequent *in vitro* and *in vivo* experiments to maximize hepatocyte-targeting efficiency.

3.2. Characterization and cellular internalization of MSN@CM-GN3

The size and polydispersity index (PDI) of optimized MSN@CM-GN3 were assessed using dynamic light scattering (DLS), and the results were shown in Fig. S6a and b. The mean particle sizes of CM, MSN, MSN@CM, and MSN@CM-GN3 were measured as 84.1 ± 4.7 nm, 95.8 ± 6.6 nm, and 98.7 ± 6.4 nm, and 110.5 ± 10.5 nm, respectively. The slight increase in hydrodynamic diameter and decrease in surface charge were indicative of successful coating (Fig. 3a). Consistent with these findings, SDS-PAGE protein electrophoresis suggested the presence of membrane proteins on the surface of MSN@CM-GN3 (Fig. 3b). Furthermore, TEM images demonstrated that MSN@CM-GN3 had a core-shell structure, with a nanoparticulate core enclosed in a thin, smooth membrane shell (Fig. 3c). Moreover, the good stability and biodegradability of MSN@CM-GN3 were confirmed in 10% FBS and H_2O_2 (Fig. 3d and S5c). To quantify the cellular uptake of MSN@CM-GN3, the corresponding fluorescence intensity was detected at different time points or concentrations. The results indicated that the fluorescence intensity of MSN@CM-GN3 increased significantly with an increase in incubation time or concentration, suggesting the outperforming internalization of MSN@CM-GN3 was time-dependent and concentration-dependent (Fig. 3e and f). Similar results were observed in HepG2 cells treated with MSN@CM-GN3 compared to MSN@CM or MSN (Fig. S7).

Considering the effect of surface ligand density of nanoparticles and receptor density of cells on the specific targeting effi-

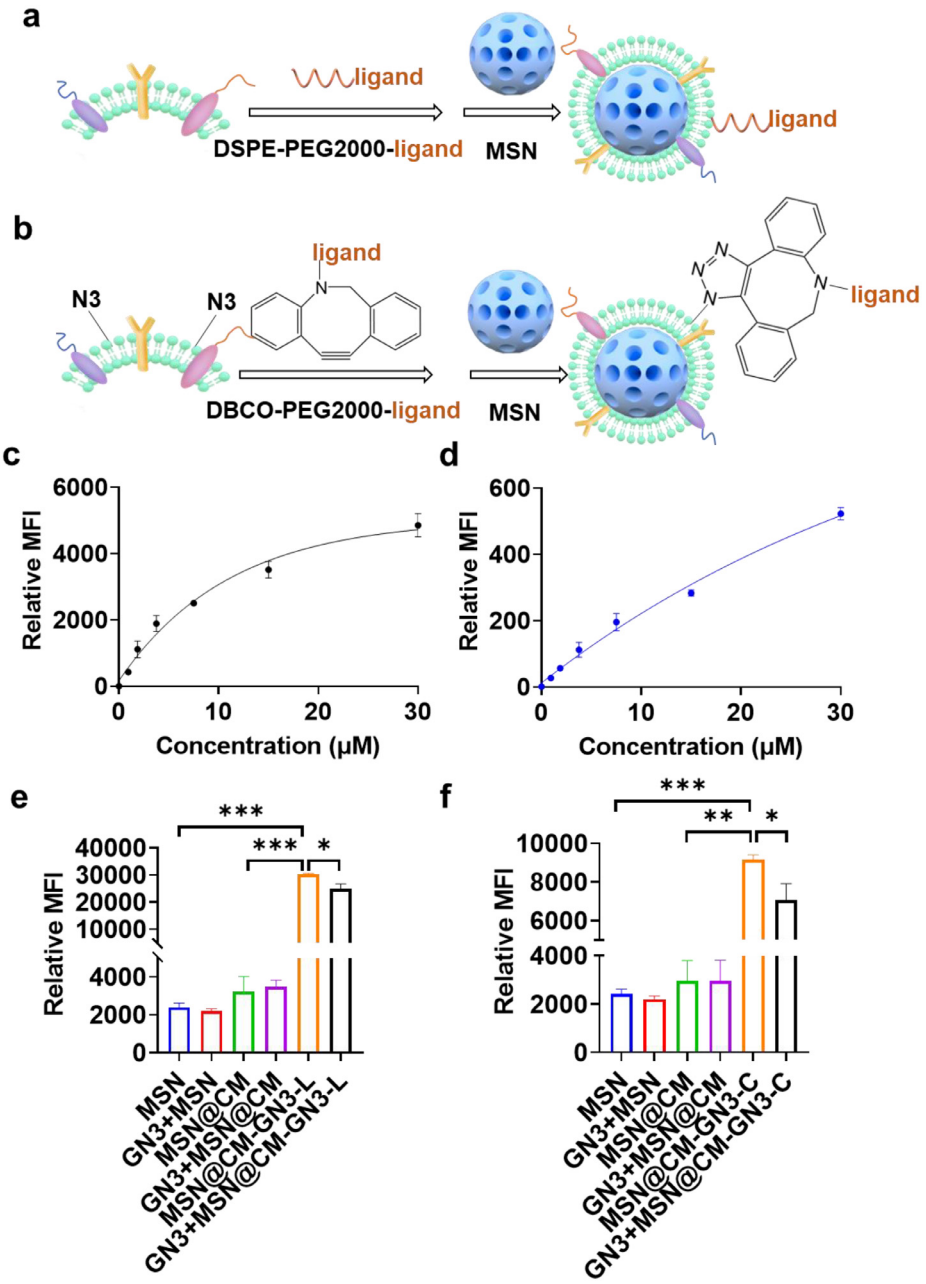

Fig. 1. Engineering GalNAc-functionalized biomimetic nanocarriers. (a, b) Schematic illustration of the preparation of MSN@CM-ligand-L and MSN@CM-ligand-C through lipid insertion and chick chemistry, respectively. (c, d) Calibration curve between the normalized mean fluorescence intensity of DSPE-PEG2000-FITC and DBCO-PEG2000-FITC-based biomimetic nanocarriers, respectively. (e, f) Cellular uptake of MSN@CM-GN3-L and MSN@CM-GN3-C were characterized by mean fluorescence intensity, respectively. Data are means ± SEM (n = 3 independent experiments; $^{*}P < 0.05$, $^{**}P < 0.01$, and $^{***}P < 0.001$ by one-way ANOVA with Tukey's multiple comparison test).

ciency [34,35], we investigated the density of receptor and ligand and in our biomimetic nanoparticles and hepatocytes, respectively. First, the MSN@CM-GN3 with high, mild and low density of ligand (defined as MSN@CM-GN3+H, MSN@CM-GN3+M, and MSN@CM-GN3+L, respectively) was fabricated. The density of GN3 ligand on the surface of the formulation was determined. The results indicated that MSN@CM-GN3+H, MSN@CM-GN3+M, and MSN@CM-GN3+L contained approximately 47127, 12241, 3795 GN3s, respectively. To assess the HepG2 cell targeting capacity of MSN@CM-GN3 with different ligand densities, we performed internalization assays. The results showed that MSN@CM-GN3 with a high density of GalNAc demonstrated significantly stronger internalization compared to MSN@CM-GN3 with medium and low density of GalNAc (Fig. 3g), in line with density-mediated cellular uptake of other ligands [36]. Beyond the GalNAc density, the quantification of ASGPR on the hepatocyte surface is crucial, which we determined by the FITC-GN3 (Scheme S3 and Fig. S8). The ASGPR expression level of HepG2 was found to be higher than Hepa1-6 and RAW264.7 cells (Fig. 3h). Furthermore, the cellular uptake of MSN@CM-GN3 in hepatocytes was in proportion to the receptor density of cell membrane (Fig. 3i), implying that the hepatic internalization of GalNAc-functionalized nanocarriers relied on receptor density. In contrast, the internalization of MSN@CM-GN3 in RAW264.7 cells was significantly lower than bare MSN, suggesting that the cell membrane coating might escape the uptake of macrophage cells. Importantly, the uptake of MSN@CM-GN3 in hepatocytes was remarkedly higher than in macrophages, demonstrating their hepatocyte-specific targeting property *in vitro*.

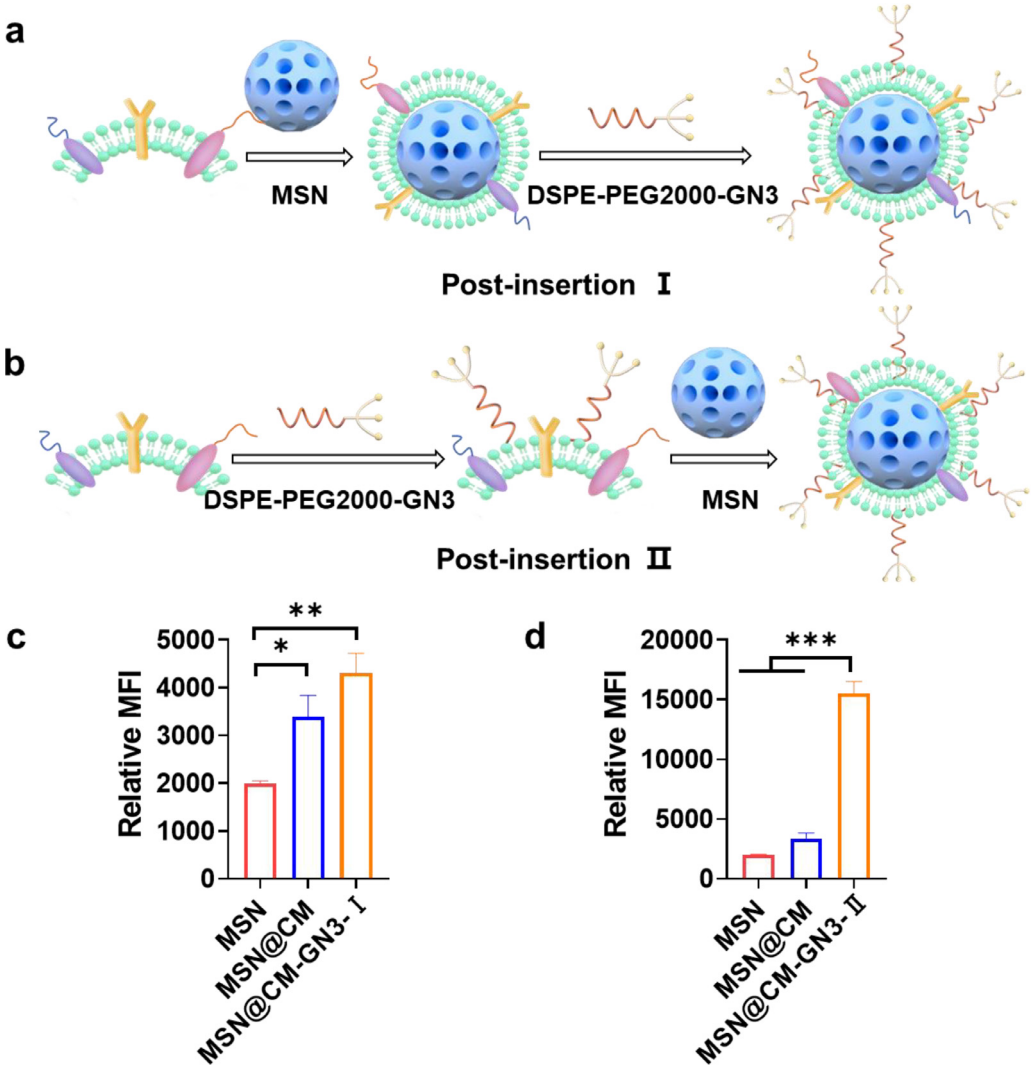

Fig. 2. GalNAc-functionalized biomimetic nanocarriers. (a, b) Schematic illustration of the fabrication of MSN@CM-GN3 by post-insertion I and II, respectively. (c, d) Determination of fluorescence intensity of HepG2 cells incubated with FITC-MSN@CM-GN3 prepared by post-insertion I and II methods, respectively. Data are means ± SEM ($n = 3$ independent experiments; $^{*}P < 0.05$, $^{**}P < 0.01$, and $^{***}P < 0.001$ by one-way ANOVA with Tukey's multiple comparison test).

Building upon our previous results, we sought to decipher the mechanism of GalNAc-mediated hepatocyte internalization. Major transport proteins have optimal activity at physiological temperatures, whereas their activity decreases at lower temperatures [37]. Compared to MSN, the cellular uptake of MSN@CM and MSN@CM-GN3 was significantly enhanced at 37 °C as opposed to 4 °C (Fig. S9), indicating the involvement of transport proteins in the internalization process. Furthermore, the substantial blocking effect of sodium azide demonstrated that the internalization of MSN@CM-GN3 relied on a strictly energy-dependent process. Importantly, we exploited several pharmacological inhibitors such as chlorpromazine (known to inhibit clathrin-mediated pathway), nystatin (a caveolae-mediated pathway blocker), and amiloride (a micropinocytosis-mediated pathway inhibitor) to block potent intracellular transport (Fig. 3j). The cellular uptake of MSN@CM-GN3 was significantly inhibited by the chlorpromazine, nystatin, and amiloride, suggesting that the involvement of clathrin-mediated endocytosis, caveolae-mediated endocytosis, micropinocytosis in the cellular uptake process. Among those pathways, clathrin-mediated endocytosis seemed to play a significant role in ASGPR-mediated endocytosis.

3.3. MSN@CM-GN3 performed hepatocyte-specific uptake and Kupffer cell escaping in vivo

To investigate the benefits of GalNAc-engineering biomimetic nanocarriers for specific targeted delivery to hepatocytes and Kupffer cells, we utilized cationic lipid nanoparticles modified with GalNAc to encapsulate MSNs (MSN@LP-GN3) as a non-cell membrane control group. *In vitro*, fluorescence intensity measurements showed that both MSN@CM-GN3 and MSN@LP-GN3 were more efficiently internalized by hepatocytes compared with MSN or MSN@CM (Fig. S10a). In contrast, a substantial amount of MSN@LP-GN3 was internalized by RAW264.7 macrophages compared to MSN@CM-GN3 (Fig. S10b). In HepG2 cells, MSN-GN3 and MSN@CM-GN3 were more efficiently internalized when compared with bare MSN (Fig. S10c). Uptake of MSN-GN3 was higher than MSN@CM-GN3 by RAW264.7 macrophages (Fig. S10d). After demonstrating the specific targeting of hepatocytes and escaping from macrophages *in vitro*, we evaluated the distribution of ICG-labeled MSN@CM-GN3 via *ex vivo* fluorescent imaging. We found that MSN@CM-GN3 was predominantly accumulated in the liver following intravenous injection (Fig. 4a). The quantitative analy-

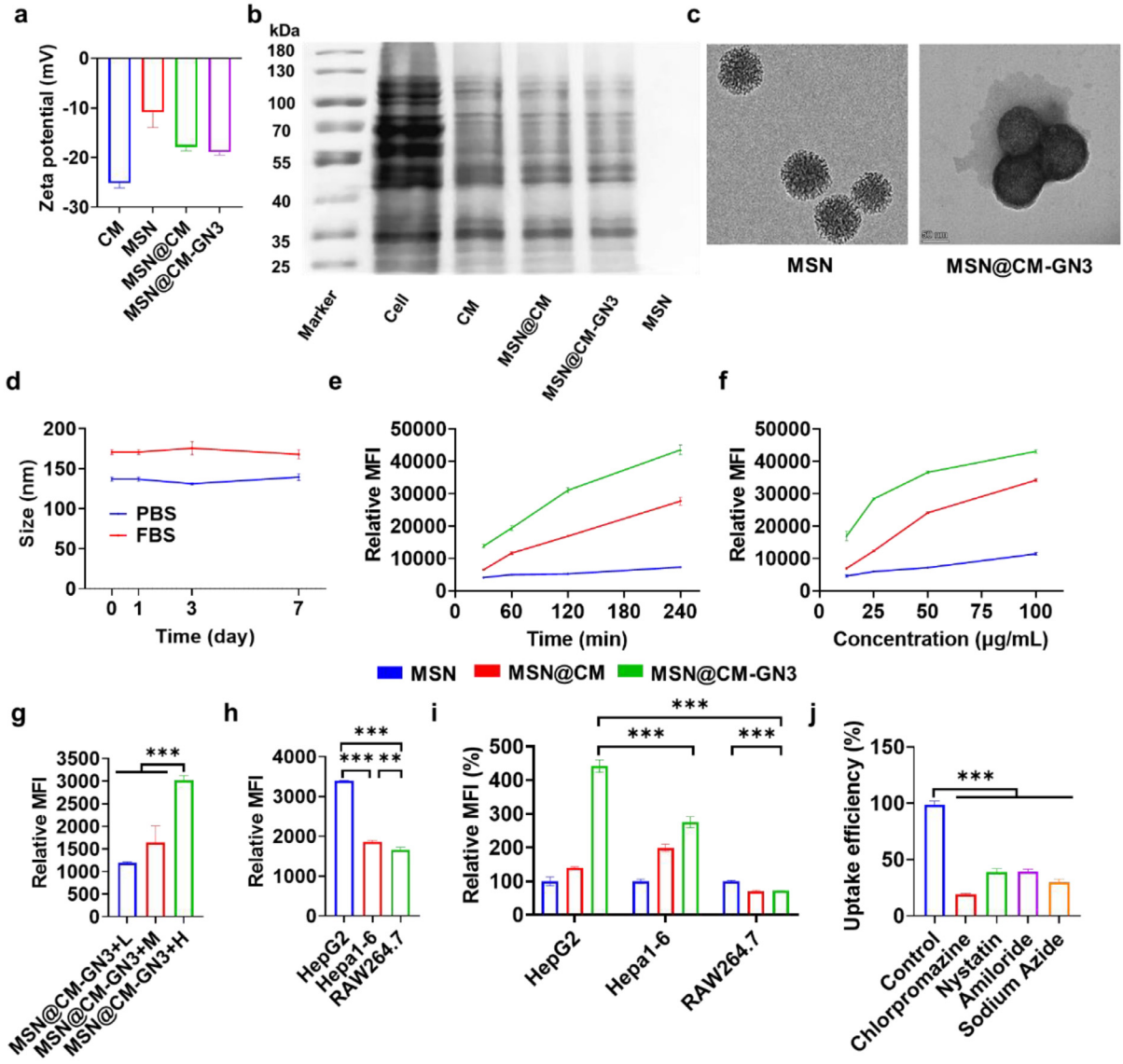

Fig. 3. Characterization and cellular uptake of MSN@CM-GN3. (a) Characterization of zeta potential. (b) SDS-PAGE analysis of protein in each group. (c) TEM images of MSN and MSN@CM-GN3. Scale bar, 50 nm. (d) Size of MSN@CM-GN3 in PBS and complete medium of 10% FBS for 7 days. (e, f) Uptake of MSN, MSN@CM, and MSN@CM-GN3 in HepG2 cells in a (e) time or (f) concentration manner, respectively. (g) The effect of GalNAc density on cell targeting. (h) Flow cytometry analysis of the ASGPR density. (i) The corresponding effect of receptor density on cell targeting in HepG2, Hepa1-6, and RAW264.7 cells, respectively. (j) Relative cellular uptake efficiency of MSN@CM-GN3 in the presence of various endocytosis inhibitors. Data are means ± SEM ($n = 3$ independent experiments; $^{*}P < 0.05$, $^{**}P < 0.01$, and $^{***}P < 0.001$ by one-way ANOVA with Tukey's multiple comparison test).

sis confirmed that MSN@CM-GN3 exhibited significantly increased liver accumulation compared to bare MSN and MSN-@CM (Fig. 4b), which may be attributed to the GalNAc-mediated hepatocyte targeting and liver first pass effect [38].

To further investigate the cell-specific distribution of MSN@CM-GN3, the fluorescence intensity of FITC-labeled biomimetic nanoparticle were evaluated in isolated primary hepatocytes and Kupffer cells (Fig. 4c). The relative mean fluorescence intensity of HCs indicated that both MSN@CM-GN3 and MSN@LP-GN3 showed considerable HCs targeting effect, which was significantly higher than MSN@CM without GalNAc-engineering (Fig. 4d). On the other hand, MSN@CM-GN3 exhibited a remarkable reduction in KCs accumulation compared to MSN@LP-GN3 and MSN (Fig. 4e). Furthermore, quantitative analysis of Ruthenium (Ru) content in HCs and KCs after administration of Ru-labeled formulations show a similar trend to that of the fluorescence intensity, where the HCs uptake of MSN@CM-GN3 was comparable to MSN@LP-GN3 (Fig. 4f), while the accumulation of MSN@CM-GN3 in KCs was consistently lower than that of MSN and MSN@LP-GN3 (Fig. 4g), which might be explained by the cell membrane coating-mediated protection to reduce non-specific RES scavenging [39]. These findings collectively suggested the selective HC-targeting ability of the MSN@CM-GN3 with reduced non-specific uptake of KCs, which highlighted its potential for HC-specific delivery as a potent nucleic acid-based therapeutic for chronic liver diseases.

3.4. Knockdown of a hepatocyte-specific gene by MSN-siRNA@CM-GN3

Given that efficient internalization and controlled release were of great importance for siRNA delivery, we encapsulated the siRNA into MSN@CM-GN3 or other formulations. We measured drug encapsulation efficiency and loading capacity, as outlined in Table S1, which indicated the satisfactory drug delivery performance of MSN@CM-GN3. We next assessed the cellular uptake efficiency and mean fluorescence intensity in HepG2 cells, which were in-

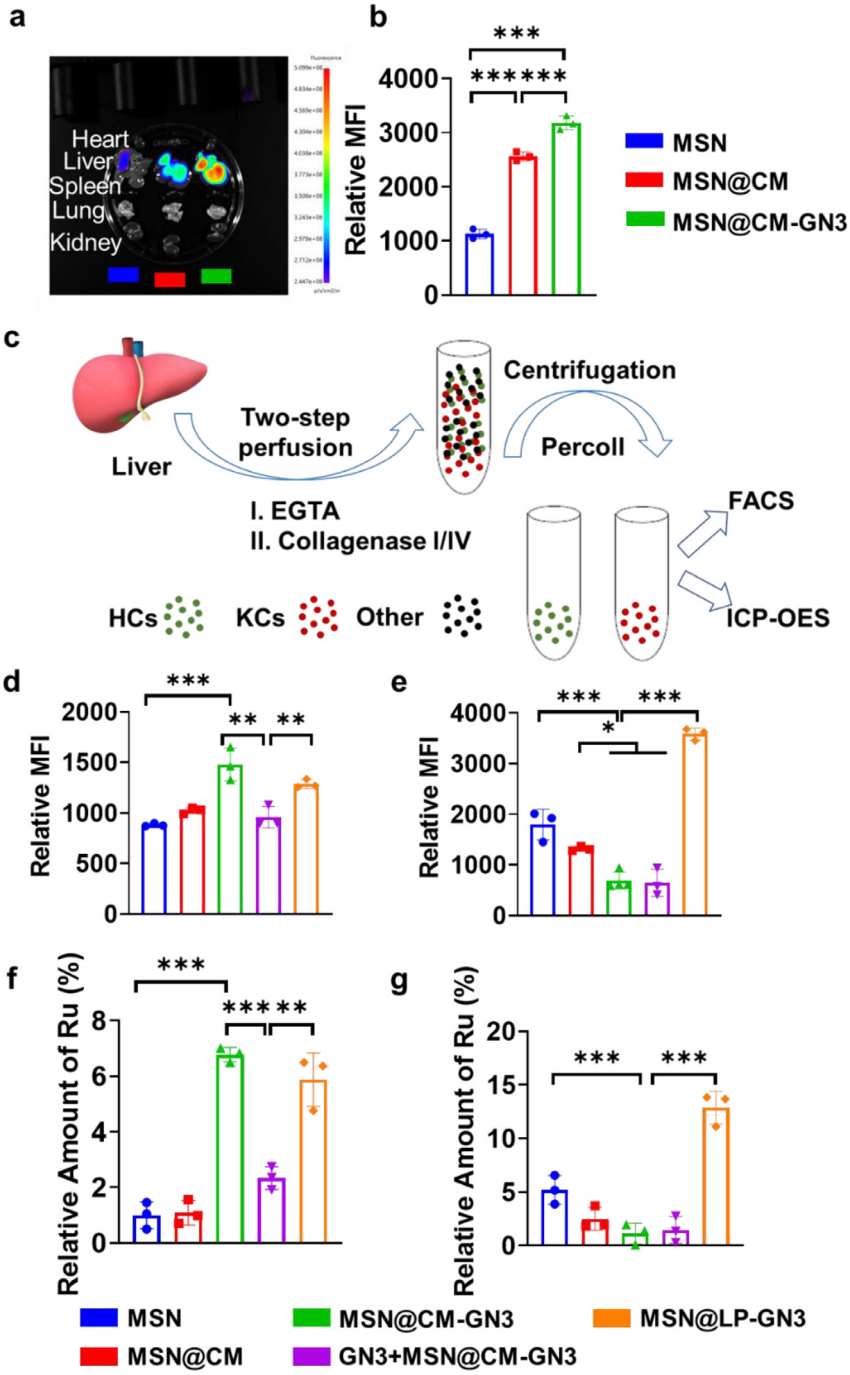

Fig. 4. Liver distribution of MSN@CM-GN3. (a) Fluorescence imaging of isolated organs (heart, liver, spleen, lung, and kidney) after intravenous injection. (b) Quantitative analysis of fluorescence intensity in the liver. (c) Schematic illustration of primary mouse HCs and KCs isolation for further flow cytometry (FACS) and inductively coupled plasma optical emission spectrometry (ICP-OES). (d, e) Flow cytometry analysis for the distribution of MSN, MSN@CM, MSN@CM-GN3, and MSN@LP-GN3 in the (d) HCs and (e) KCs, respectively. (f, g) ICP analysis for determining the Ru content of MSN, MSN@CM, MSN@CM-GN3, and MSN@LP-GN3 in the (f) HCs and (g) KCs, respectively. Data are means ± SEM ($n = 3$ independent experiments; $^{*}P < 0.05$, $^{**}P < 0.01$, and $^{***}P < 0.001$ by one-way ANOVA with Tukey's multiple comparison test).

cubated with Cy5-labeled siRNA-loaded nanocarriers for 4 h (Fig. S11a). The results indicated that GalNAc-functionalized membrane-coated nanocarriers enhanced the cellular uptake and internalized efficiency of siRNA (Fig. S11b and c). The gene silencing efficiency of PCSK9 was evaluated *in vitro* and *in vivo* to further evaluate the delivery performance of MSN@CM-GN3 (Fig. 5a). Amine-modified MSNs were utilized to encapsulate siRNA to fabricate MSN/siRNA@CM-GN3 with varying MSN/siRNA ratio from 100:1 to 10:1 (w: w). HepG2 cells were transfected with MSN/siRNA at differing ratios, and RT-qPCR was performed to determine the relative mRNA expression of PCSK9 and its downregulated LDLR. The data demonstrated that MSN/siRNA@CM-GN3 significantly suppressed PCSK9 mRNA expression, while significantly up-regulated LDLR expression at the ratio of 50:1 (MSN: siRNA, w: w) (Fig. S11d and e). The MSN/siRNA@CM-GN3 showed an average diameter about 170 nm (Fig. S11f), which is considerable to that of MSN @CM-GN3 (Fig. S6a). This result indicated that siRNA loading MSN core had litter influence effects on the CM coating on the surface. Thus, we chose this condition to perform further experiments. Compared to free siRNA-treated cells, MSN/siRNA@CM-GN3 dramatically in-

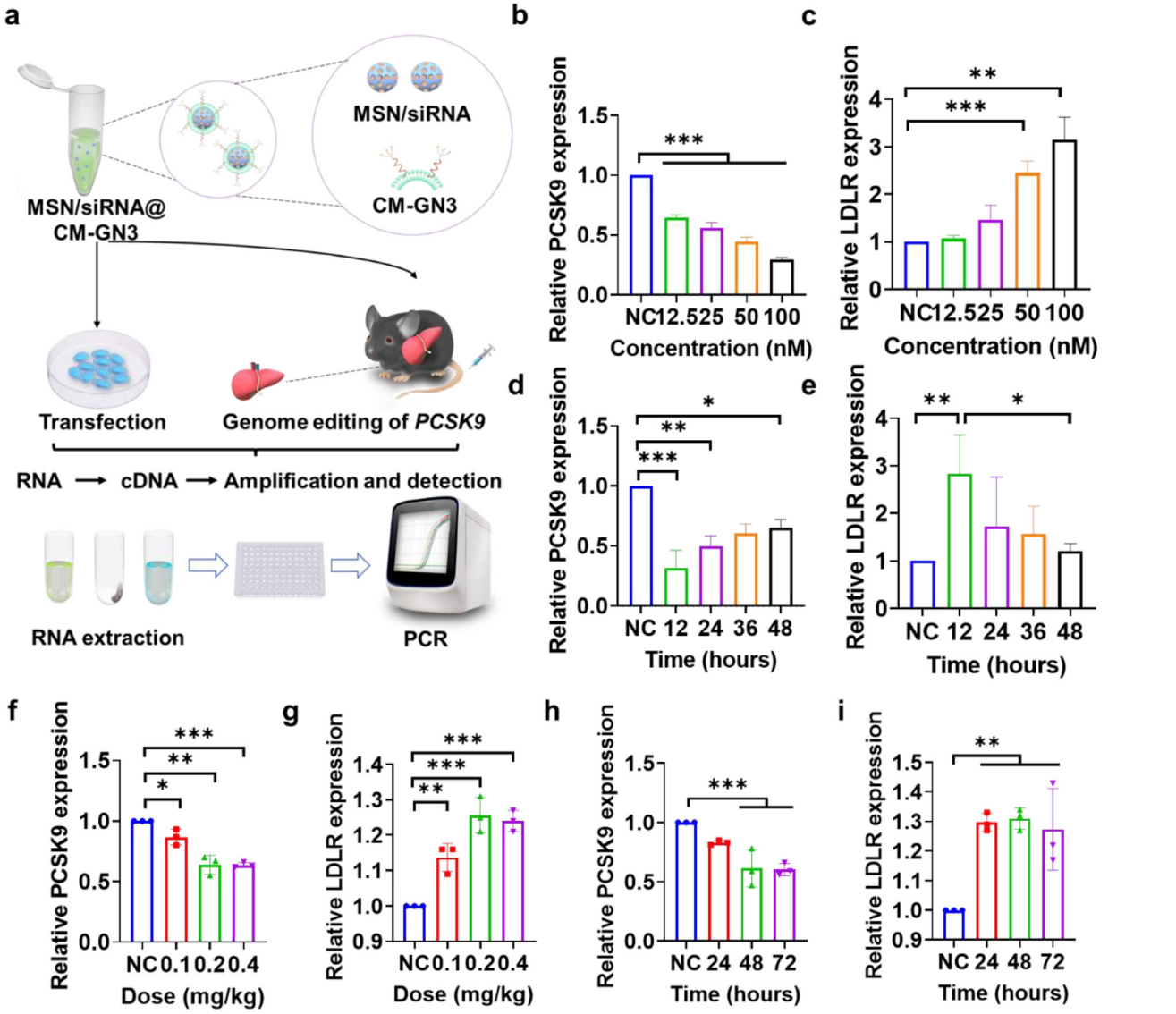

Fig. 5. Transfection efficiency of MSN/siRNA@CM-GN3 *in vitro* and *in vivo*. (a) Schematic illustration of gene silencing process both *in vitro* and *in vivo*. (b, c) RT-qPCR validation of (b) PCSK9 and (c) LDLR mRNA expression level in the HepG2 cells relative to the untreated control after normalization to GAPDH expression, respectively. (d, e) RT-qPCR validation of (d) PCSK9 and LDLR (e) mRNA expression level at differing transfection times. (f, g) Relative (f) PCSK9, and (g) LDLR mRNA expression in the liver after administration of 0.1, 0.2, and 0.4 mg/kg dose, respectively. (h, i) The levels of (h) PCSK9 and (i) LDLR expression in the liver at indicated time points. Data are means ± SEM ($n = 3$ independent experiments; $^{*}P < 0.05$, $^{**}P < 0.01$, and $^{***}P < 0.001$ by one-way ANOVA with Tukey's multiple comparison test).

hibited PCSK9 mRNA expression and facilitated LDLR mRNA expression in a concentration-dependent manner (Fig. 5b and c). In particular, HepG2 cells transfected with MSN/siRNA@CM-GN3 achieved almost 60% knockdown of PCSK9 mRNA expression. Furthermore, PCSK9 mRNA expression in HepG2 cells decreased with the extension of transfection time, while LDLR mRNA expression was increased at the same time (Fig. 5d and e). These results indicated the time-dependent gene silencing by MSN/siRNA@CM-GN3. In addition, DLin-MC3-DMA LNP has been approved for siRNA therapeutics. A knockdown activity study was conducted in HepG2 cells comparing MC3-LNP to MSN@CM-GN3. The results demonstrated that both siRNA@MC3-LNP and MSN/siRNA@CM-GN3 exhibited robust gene therapeutic efficiency (Fig. S12a and b).

To further evaluate the *in vivo* gene therapeutic efficiency of MSN@CM-GN3, mice were grouped and administered MSN/siRNA@CM-GN3 intravenously at a dose of 0.1 mg/kg, 0.2 mg/kg, and 0.4 mg/kg. The dose-dependent effects of the nanocarrier on PCSK9 and LDLR mRNA expression in the liver were evaluated (Fig. 5f and g). Consistently, PCSK9 mRNA expression was suppressed, and LDLR mRNA expression was enhanced in a dose-dependent manner. Additionally, the expression of PCSK9 and LDLR mRNA expression was measured at different time points (24, 48, and 72 h) (Fig. 5h and i). Gene silencing was observed for each time point with the peak silencing occurring at 48 h. Importantly, both MSN/siRNA@CM-GN3 and siRNA@MC3-LNP were intravenously administered to mice, demonstrating considerable gene therapy efficiency in the liver (Fig. S12c and d). Taken together, these findings demonstrated that MSN/siRNA@CM-GN3 efficiently silenced gene expression in hepatocytes and the liver, indicating its potential use in the treatment of liver diseases.

3.5. Hepatocyte-specific siRNA-dependent PCSK9 deletion in HFD-induced NAFLD model with good biocompatibility

NAFLD is considered one of the leading causes of liver disease-related mortality worldwide and is probably associated with increased cardiovascular mortality [40,41]. Currently, RNAi-based lipid-lowering has emerged as an attractive strategy for reduc-

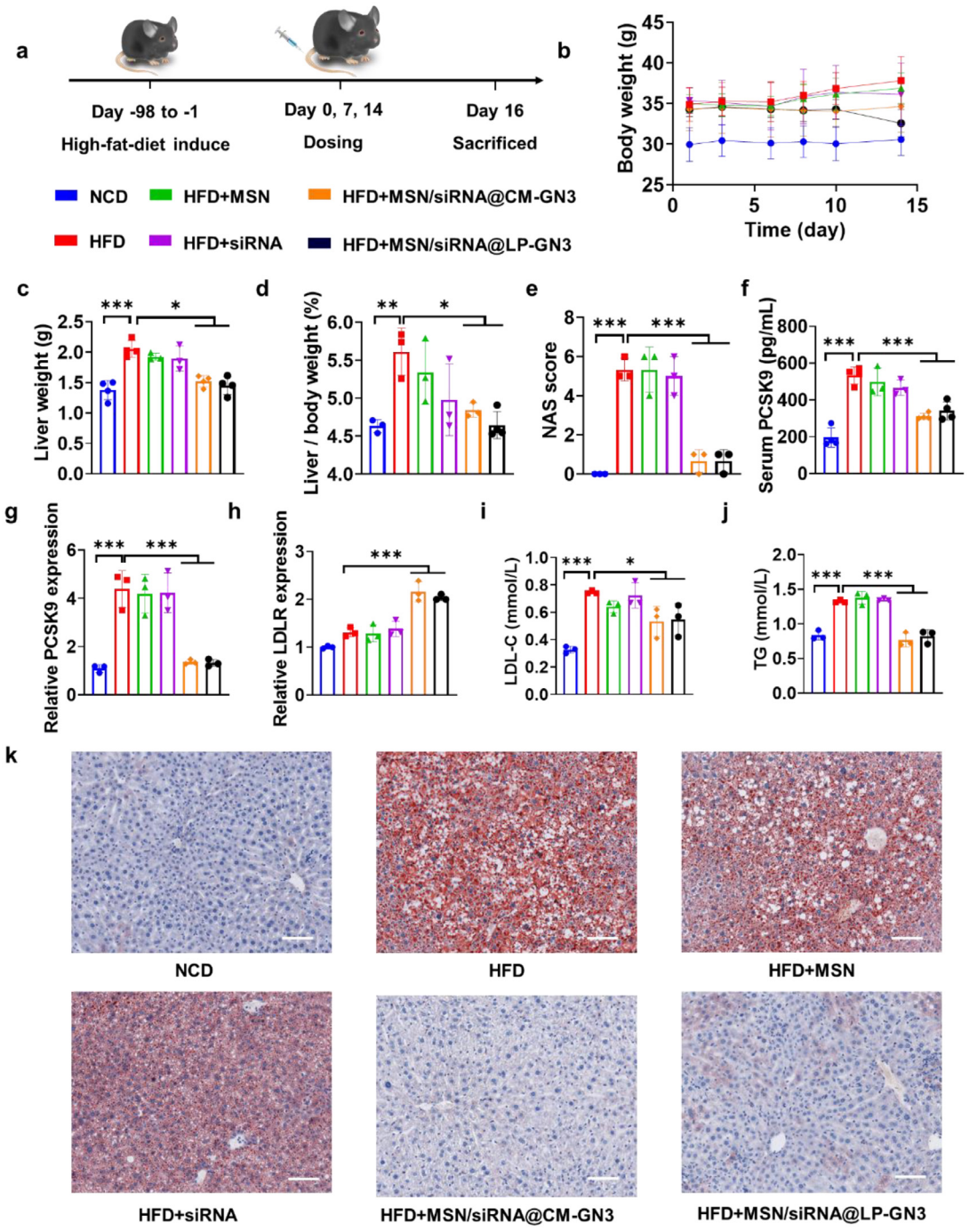

Fig. 6. Therapeutic efficacy of MSN/siRNA@CM-GN3 in HFD-induced mice. (a) Scheme illustration of the therapeutic schedule. (b) Body weight changes, (c) liver weight, and (d) liver/body weight ratio during the treatment. (e) NAFLD activity scores (NAS) of steatoses, lobular inflammation, and ballooning for each group. (f) ELISA analysis of the serum PCSK9 content. (g, h) RT-qPCR analysis of (g) PCSK9 and (h) LDLR mRNA expression in the liver. (i, j) Levels of serum LDL-C and TG at the end of treatment, respectively. (k) Oil red O staining of the liver tissues of each group. Scale bar, 100 μm. Data are means ± SEM (n = 3–4 independent experiments; $^{*}P < 0.05$, $^{**}P < 0.01$, and $^{***}P < 0.001$ by one-way ANOVA with Tukey's multiple comparison test).

ing LDL-C levels by silencing PCSK9 [42]. To further assess the therapeutic effects of MSN/siRNA@CM-GN3, the NAFLD mice model was established through long-term exposure to a high-fat diet. Subsequently, animals were treated once per week with MSN/siRNA@CM-GN3 or other formulations (PBS, MSN, siRNA, and MSN/siRNA@LP-GN3) according to the illustration (Fig. 6a). The body weight of animals treated with MSN/siRNA@CM-GN3 grew slowly during the first two weeks of treatment in contrast to the HFD model group (Fig. 6b). However, the body weight of the MSN/siRNA@LP-GN3 group decreased rapidly after the third injection. At the end of MSN/siRNA@CM-GN3 treatment, liver weight, and liver/body weight ratio decreased remarkably compared to PBS, siRNA, and MSN-treated animals (Fig. 6c and d). Since epididymal adipose tissues are associated with the progression of NAFLD [43], we also observed significantly lower epididymal adipose tissue weight and smaller adipocyte diameter in MSN/siRNA@CM-GN3 and MSN/siRNA@LP-GN3 groups (Fig. S13).

Hematoxylin and eosin (H&E) staining of the liver tissues showed that the HFD-fed mice had numerous vacuoles (Fig. 6e and S14). However, both MSN/siRNA@CM-GN3 and MSN/siRNA@LP-

GN3-treated mice exhibited no significant steatosis, lobular inflammation, or hepatocyte ballooning compared to siRNA and MSN-treated animals. The remarked reduction of serum PCSK9 level and PCSK9 mRNA in the liver was observed in MSN/siRNA@CM-GN3 and MSN/siRNA@LP-GN3 treated animals (Fig. 6f and g). The PCSK9 mRNA expression decreased, accompanied by an increase in LDLR mRNA expression (Fig. 6h). Furthermore, LDL-C, TG, and TC in the serum and liver of MSN/siRNA@CM-GN3-treated mice remained within the normal range in contrast to HFD-induced mice (Fig. 6i, j and S15). The treatment of MSN/siRNA@CM-GN3 and MSN/siRNA@LP-GN3 led to fewer lipid droplet accumulation in the cytoplasm, as revealed by oil red O staining (Fig. 6k). Collectively, these therapeutic performances demonstrated the robust PCSK9 gene inhibition of both MSN/siRNA@CM-GN3 and MSN/siRNA@LP-GN3 in HFD-induced mice.

The body weight data shown in Fig. 6b indicated that repeated administration of MSN/siRNA@LP-GN3 may be associated with potential toxicity. This was further confirmed by the H&E staining of MSN/siRNA@LP-GN3-treated mice, which revealed significant liver necrosis (Fig. 7a and Fig. S16). In addition, the H&E staining of the liver, heart, spleen, lung, and kidney yielded no observable damage in all treatment groups (Fig. S17), indicating that the repeated administration of MSN/siRNA@CM-GN3 did not induce any obvious toxicity. Consistent with these *in vivo* safety profiles, cell viability assays at a final concentration of 400 μg/mL demonstrated that MSN@CM-GN3 treatment showed no significant impact on the viability of RAW264.7 cells, Fibroblast cells (L929) and HUVECs (Fig. 7b-d). However, MSN@LP-GN3-treated cells exhibited significant toxicity compared to PBS-treated cells. To further determine the potential toxicity of MSN/siRNA@LP-GN3, the levels of serum ALT, AST, and TNF-α in the serum and liver indicated that only repeated administration of MSN/siRNA@LP-GN3 resulted in significant adverse effects (Fig. 7e-h), possibly due to the static interaction with proteins on the cationic nanoparticulate surface. Overall, these findings demonstrated that MSN/siRNA@CM-GN3 has a safe potential for long-term treatment of NAFLD.

4. Discussion

Efficient management of chronic liver diseases remained a great challenge due to the lack of curative therapeutic options [44,45]. RNAi has been recognized as a promising approach for third-generation drug development, with LNPs being the most widely used carrier in clinic settings [46]. However, the application of LNPs has been hindered by issues such as undesirable stability, hepatoxicity, and non-specific uptake of KCs. The ligand GalNAc has been found to exhibit a high binding affinity for ASGPR, which is overexpressed on hepatocytes [47]. This GalNAc/ASGPR relationship has prompted the development of GalNAc-functionalized nanoplatforms for selective hepatocyte targeting, though they are still subject to non-specific capture by RES. Incorporated cell membrane coating into nanocarriers provides the macrophage-escaping ability and prolongs systematic circulation time [48,49], making it possible to design a GalNAc-functionalized biomimetic system that can delivery small interfering RNA with high efficiency and safety for hepatocyte-specific targeting.

An important variable in developing the GalNAc-functionalized biomimetic system was the engineering strategy employed. To normalize the amount of GalNAc incorporated into the cell membrane, we employed the GalNAc-to-membrane protein ratio as a useful metric. Herein, we generated biomimetic nanoformulations using covalent or non-covalent methods with identical GalNAc-to-membrane protein ratios, followed by sonication-based coating. To assess the impact of the engineering strategy on the biofunctional characteristic, we quantitatively compared cellular uptake. The primary hepatocytes can exhibit higher ASGPR receptor expression than cancer cell lines, their expression was unstable due to readily loss of their phenotype culturing in vitro, which was harmful for evaluation of receptor-mediated uptake. Thus, we chose HepG2 and Hepa1-6 cells for the evaluation of cellular uptake. Our findings demonstrated that the pathways through which the GalNAc is functionalized affect the cellular uptake of nanoparticles. Nanocarriers generated through lipid insertion exhibited increased uptake, which was consistent with the higher engineering efficiency. However, the azide-modified cell membrane vesicles for click chemistry were obtained through culture with azide-modified molecules, as previously reported, and subsequently conjugated with DBCO-modified ligands [50,51]. The functionalized efficiency of this two-step process might be challenged due to the low engineering efficiency when compared with one-step insertion.

Lipid insertion relies on physical interactions by exploiting the fluidity of membranes [52]. The fluidity of the cell membrane on the surface of nanoparticles was probably decreased compared to that of bare cell membrane vesicles. The low cellular uptake of the biomimetic system prepared by lipid insertion I might be affected by the fluidity or integrity of the cell membrane. Moreover, the low efficient insertion of by lipid insertion I method might led the direction of GalNAc to the inside rather than outside. Therefore, cell membrane vesicles were functionalized with GalNAc previously and then coated on the MSN might be the best insertion order for drug delivery. Furthermore, the differing cell membrane types (macrophages and borrow mesenchymal stem cells) were selected to construct a biomimetic system to reduce immunogenicity. We observed that both of these types of cell membranes coated nanocarriers functionally delivered nanoparticles to HepG2 cells, demonstrating that the GalNAc-functionalized system approach could be widely used for different cell types. Interestingly, we observed that the cellular uptake of MSN coated with macrophage membrane was more potent than that of MSN coated with the stem cell membrane. However, this apparent discrepancy could be due to multiple variables such as the production process and the intrinsic characteristic of homing, which required further investigation. By optimizing the insertion order and cell membrane source, we obtained outperforming GalNAc-functionalized nanoformulations via lipid insertion.

The GalNAc-functionalized biomimetic system exhibited a time- and dose-dependent internalization in HepG2 cells, with the cellular uptake being influenced by various factors, including GalNAc density, ASGPR density, and cell membrane type. To optimize the nanoplatform, it is important to balance the fluidity of the biomimetic system and the saturation of the receptor. We found that nanoplatforms generated with higher GalNAc density compromised with good fluidity of CM-GN3 exhibited a positive effect on hepatocyte targeting. The cellular uptake of MSN@CM-GN3 was positively relevant to the receptor density on the cell membrane and enhanced uptake of nanoparticles was partially attributed to ASGPR-mediated endocytosis. Clathrin-mediated endocytosis was the predominant uptake mechanism of MSN@CM-GN3, consistent with previous studies [28,37]. We investigated the uptake efficiency of MSN@CM-GN3, along with MSN@LP-GN3 as a widely used carrier in small interfering RNA delivery [11,53]. MSN@CM-GN3 and MSN@LP-GN3 were both effectively taken up in HepG2 cells, but MSN@LP-GN3 showed greater accumulation than MSN@CM-GN3 in RAW264.7 cells, likely due to the predominantly uptake of macrophages for cationic liposomes [17,54]. Both MSN@CM-GN3 and MSN@LP-GN3 exhibited similar efficiency *in vivo*, but MSN@CM-GN3 demonstrated strong hepatocyte-specific delivery and Kupffer cell escaping, suggesting promising advantages for hepatocyte-specific gene delivery.

The functional delivery of siRNA by MSN@CM-GN3 showed a dual-time and dose-dependent manner *in vitro* and *in vivo,* with

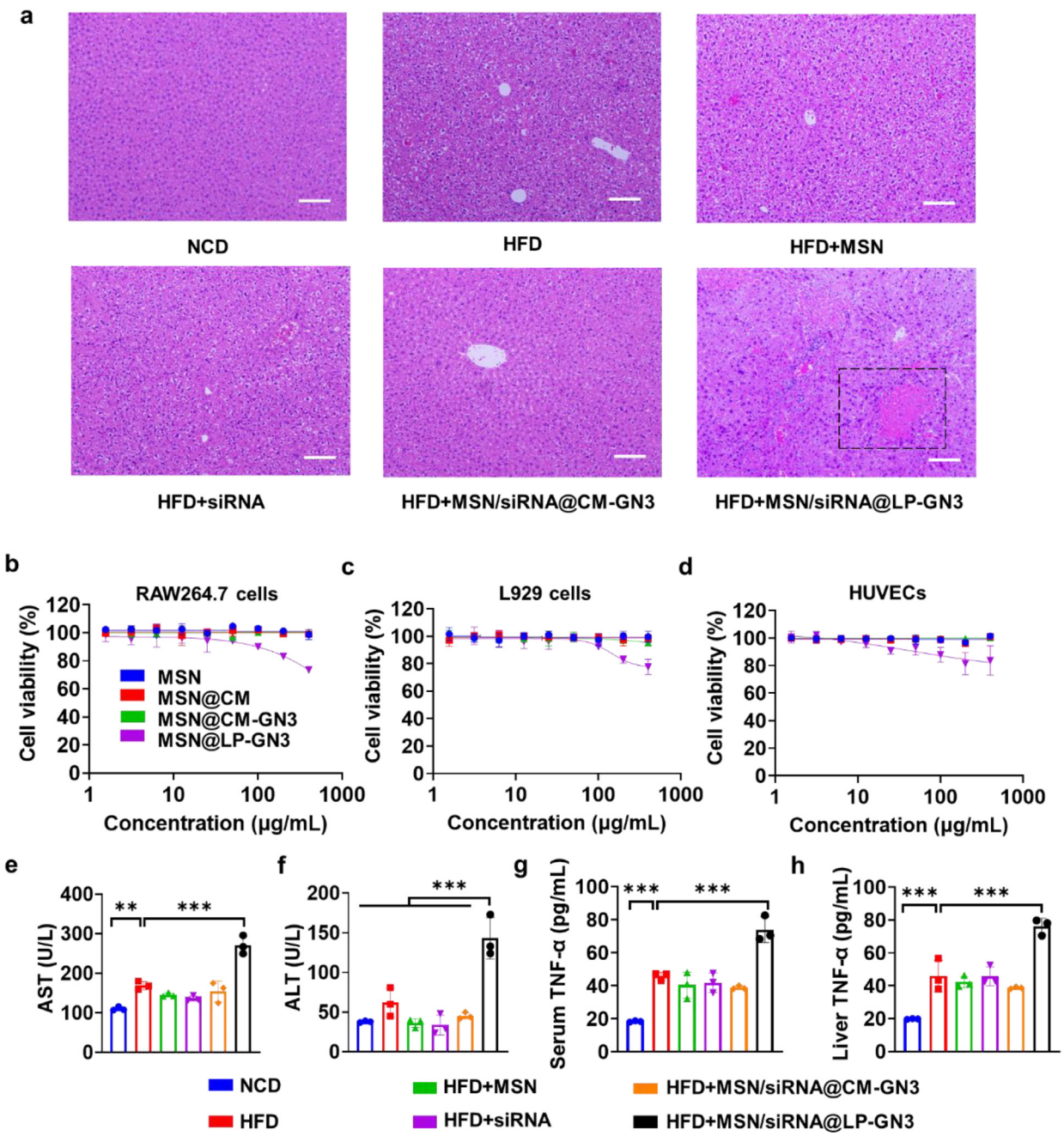

Fig. 7. The safety profile of MSN/siRNA@CM-GN3 *in vitro* and *in vivo*. (a) H&E staining of the liver sections of each group. Scale bar, 100 μm. (b-d) Cell viabilities of MSN, MSN@CM, MSN@CM-GN3, and MSN@LP-GN3 were evaluated using (b) RAW264.7 cells, (c) L929 cells, and (d) HUVECs, respectively. (e, f) Serum (e) AST and (f) ALT were measured, respectively. (g, h) Measurement of TNF-α in the (g) serum and (h) liver, respectively. Data are means ± SEM (n = 3 independent experiments; $^{*}P < 0.05$, $^{**}P < 0.01$, and $^{***}P < 0.001$ by one-way ANOVA with Tukey's multiple comparison test).

the highest knockdown achieved at a specific time point. However, a direct comparison of the activity of siRNA delivery nanoplatforms required further investigation of the pharmacokinetics of nanoplatforms. MSN@CM-GN3 exhibited superior *in vivo* gene expression knockdown, resulting in effective lipid-lowering performance in the HFD-induced NAFLD model. Both MSN@CM-GN3 and MSN@LP-GN3 exhibited considerable effects on PCSK9 gene therapy. Hepatotoxicity was a major concern for cationic liposomes used for RNA delivery, which might be relevant to innate immune activation [55]. To address these concerns, cell membrane vesicles were generally considered to lower immunogenicity and toxicity in previous studies [56–58]. MSN@CM-GN3 demonstrated good biocompatibility *in vitro* and *in vivo* compared to MSN@LP-GN3 for repeated doses, highlighting their promising potential for safe and efficient hepatocyte-specific siRNA delivery with selective hepatocyte targeting ability and escaping from non-specific RES capture. However, further preclinical studies in large animal models were required to optimize the treatment regimen for MSN@CM-GN3-based gene delivery before clinical testing.

Following the introduction of DLin-MC3-DMA, LNP technology was initially utilized for small nucleic acid drug delivery, with Onpattro receiving market approval and making LNP the most extensively used RNA delivery technology of that period. The success of Alnylam's Patisiran exemplified the potential of LNP as a carrier for small nucleic acid drugs. However, the toxicity of ionizable cations in LNPs posed a significant obstacle, limiting their

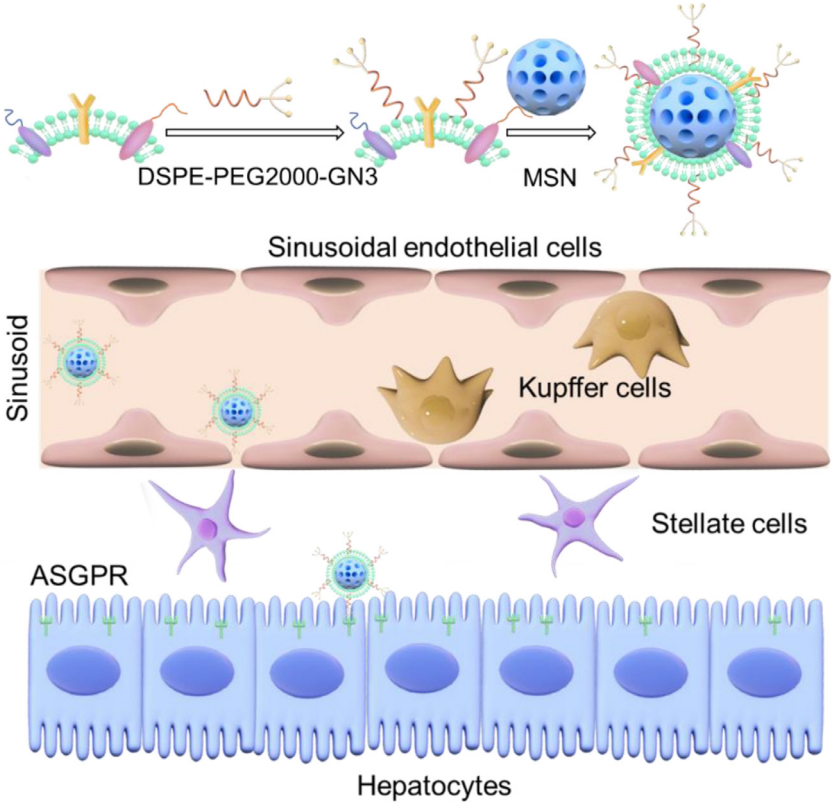

Scheme 1. The schematic illustration of the fabrication procedure of biomimetic system for hepatocyte-specific delivery.

maximum dosage and necessitating prolonged monitoring of their long-term side effects. In this context, the development of novel nanoplatforms with degradability, low toxicity, and organ-specific targeting capabilities was a promising direction for research and development. Our delivery formulation (MSN@CM-GN3) was compared to a positive control formulation (MSN@LP-GN3) containing DSPC, DLin-MC3-DMA, cholesterol, and PEG-lipid. Compared with MSN@LP-GN3, MSN@CM-GN3 exhibited strong hepatocyte targeting and Kupffer cell escaping, as well as good biocompatibility for safe and efficient siRNA delivery. Furthermore, siPCSK9 delivered by MSN@CM-GN3 reduced both serum and liver LDL-C, TG, TC levels and lipid droplets in HFD-induced mice, resulting in better performance than MSN/siPCSK9@LP-GN3 in terms of lipid-lowering effect and safety profiles. In addition, a comparative study of gene therapy activity has been conducted in mice using MC3 LNP and GalNAc-siRNA conjugate [59]. The results illustrated that MC3 LNP-mediated gene silencing was higher than that of GalNAc-siRNA due to the specific pharmacokinetics property of GalNAc-siRNA, with the highest knockdown usually occurring on days 7-14 after subcutaneous injection. However, to directly compare the gene therapeutic efficiency of siRNA delivery platforms, the samples were collected at 48 h. These findings indicated promising advantages of our biomimetic GN3-based systems for hepatocyte-specific gene delivery in chronic liver diseases (Scheme 1).

5. Conclusion

In conclusion, we introduced a promising hepatocyte-targeting nanoplatform for robust gene therapy, which enabled efficient and safe treatment of NAFLD. This easy-to-fabricate delivery system leverages the biodegradable MSN core to load siRNA or other biomolecular cargos, while the cell membrane coating provided consistent and predictable characteristics to reduce non-specific delivery. Importantly, the integration of the Tris-GalNAc ligand with the cell membrane through ordered lipid insertion allowed specific hepatocyte targeting and internalization. The *in vitro* and *in vivo* gene disruption results provided encouraging evidence that MSN@CM-GN3 exhibited considerable performance when compared with cationic MSN@LP-GN3. Consequently, data manifested that the siPCSK9 delivered by MSN@CM-GN3 reduced both serum and liver LDL-C, TG, and TC levels in HFD-induced mice, resulting in better performance than MSN/siPCSK9@LP-GN3 in lipid-lowing effect and safety profiles. Our work addressed the challenges of lower targeting efficiency of cell membrane-mimetic drug delivery systems and the immunogenicity of traditional GalNAc delivery systems. The rational design of sophisticated ligand-engineering biomimetic nanoplatforms by precisely regulating the optimal ligand on the cell membrane-coated nanoparticulate core explored fruitful applications in achieving cell-selective targeting and reducing non-specific clearance. Collectively, this study provided an effective and versatile approach for efficient and safe gene therapy using ligand-integrated biomimetic nanoplatforms.

Declaration of Competing Interest

These authors declare no conflict of interest.

CRediT authorship contribution statement

Xuan He: Methodology, Data curation, Writing – original draft. **Zhimin Chang:** Funding acquisition, Methodology, Writing – original draft. **Fangman Chen:** Investigation, Data curation, Writing – review & editing. **Wensheng Zhang:** Methodology. **Madi Sun:** Methodology. **Tongfei Shi:** Methodology, Software. **Jie Liu:** Methodology. **Peiyu Chen:** Methodology, Software, Validation. **Kunbao Zhang:** Methodology. **Shan Guan:** Methodology. **Zhibin Zhao:** Methodology, Validation. **Mingqiang Li:** Methodology. **Wen-fei Dong:** Resources, Methodology. **Dan Shao:** Funding

acquisition, Supervision, Writing – review & editing. **Chao Yang:** Methodology, Conceptualization, Funding acquisition, Writing – review & editing.

Acknowledgements

This work was supported by the Natural Science Foundation of Guangdong Province, China (No. 2021A1515010408) and National Natural Science Foundation of China (32271388).

Supplementary materials

Supplementary material associated with this article can be found, in the online version, at doi:10.1016/j.actbio.2023.10.038.

References

[1] S.K. Asrani, H. Devarbhavi, J. Eaton, P.S. Kamath, Burden of liver diseases in the world, J. Hepatol. 70 (1) (2019) 151–171.
[2] Y. Ye, H. Wang, J. Gao, E. Kostallari, Editorial: Chronic liver disease: new targets and new mechanisms, Front. Mol. Biosci 9 (2022) 963630.
[3] D. Adams, A. Gonzalez-Duarte, W.D. O'Riordan, C.C. Yang, M. Ueda, A.V. Kristen, I. Tournev, H.H. Schmidt, T. Coelho, J.L. Berk, K.P. Lin, G. Vita, S. Attarian, V. Planté-Bordeneuve, M.M. Mezei, J.M. Campistol, J. Buades, T.H. Brannagan 3rd, B.J. Kim, J. Oh, Y. Parman, Y. Sekijima, P.N. Hawkins, S.D. Solomon, M. Polydefkis, P.J. Dyck, P.J. Gandhi, S. Goyal, J. Chen, A.L. Strahs, S.V. Nochur, M.T. Sweetser, P.P. Garg, A.K. Vaishnaw, J.A. Gollob, O.B. Suhr, Patisiran, an RNAi therapeutic, for hereditary transthyretin amyloidosis, N. Engl. J. Med. 379 (1) (2018) 11–21.
[4] H.H. Schmidt, J. Wixner, V. Planté-Bordeneuve, F. Muñoz-Beamud, L. Lladó, J.D. Gillmore, A. Mazzeo, X. Li, S. Arum, P.Y. Jay, D. Adams, Patisiran treatment in patients with hereditary transthyretin-mediated amyloidosis with polyneuropathy after liver transplantation, Am. J. Transplant. 22 (6) (2022) 1646–1657.
[5] H. Li, Y. Fu, T. Zhang, Y. Li, X. Hong, J. Jiang, T. Gong, Z. Zhang, X. Sun, Rational design of polymeric hybrid micelles with highly tunable properties to co-deliver MicroRNA-34a and vismodegib for melanoma therapy, Adv. Funct. Mater. 25 (48) (2015) 7457–7469.
[6] Q. Wang, H. Jiang, Y. Li, W. Chen, H. Li, K. Peng, Z. Zhang, X. Sun, Targeting NF-kB signaling with polymeric hybrid micelles that co-deliver siRNA and dexamethasone for arthritis therapy, Biomaterials 122 (2017) 10–22.
[7] X. Chen, L.S. Mangala, C. Rodriguez-Aguayo, X. Kong, G. Lopez-Berestein, A.K. Sood, RNA interference-based therapy and its delivery systems, Cancer Metast. Rev. 37 (1) (2018) 107–124.
[8] C. Lorenzer, M. Dirin, A.-M. Winkler, V. Baumann, J. Winkler, Going beyond the liver: Progress and challenges of targeted delivery of siRNA therapeutics, J. Control. Release 203 (2015) 1–15.
[9] S.M. Hammond, A. Aartsma-Rus, S. Alves, S.E. Borgos, R.A.M. Buijsen, R.W.J. Collin, G. Covello, M.A. Denti, L.R. Desviat, L. Echevarría, C. Foged, G. Gaina, A. Garanto, A.T. Goyenvalle, M. Guzowska, I. Holodnuka, D.R. Jones, S. Krause, T. Lehto, M. Montolio, W. Van Roon-Mom, V. Arechavala-Gomeza, Delivery of oligonucleotide-based therapeutics: challenges and opportunities, EMBO Mol. Med 13 (4) (2021) e13243.
[10] S. Kamerkar, V.S. LeBleu, H. Sugimoto, S. Yang, C.F. Ruivo, S.A. Melo, J.J. Lee, R. Kalluri, Exosomes facilitate therapeutic targeting of oncogenic KRAS in pancreatic cancer, Nature 546 (7659) (2017) 498–503.
[11] S.C. Semple, A. Akinc, J. Chen, A.P. Sandhu, B.L. Mui, C.K. Cho, D.W.Y. Sah, D. Stebbing, E.J. Crosley, E. Yaworski, I.M. Hafez, J.R. Dorkin, J. Qin, K. Lam, K.G. Rajeev, K.F. Wong, L.B. Jeffs, L. Nechev, M.L. Eisenhardt, M. Jayaraman, M. Kazem, M.A. Maier, M. Srinivasulu, M.J. Weinstein, Q. Chen, R. Alvarez, S.A. Barros, S. De, S.K. Klimuk, T. Borland, V. Kosovrasti, W.L. Cantley, Y.K. Tam, M. Manoharan, M.A. Ciufolini, M.A. Tracy, A. de Fougerolles, I. MacLachlan, P.R. Cullis, T.D. Madden, M.J. Hope, Rational design of cationic lipids for siRNA delivery, Nat. Biotechnol. 28 (2) (2010) 172–176.
[12] C. Qiu, H.H. Han, J. Sun, H.T. Zhang, W. Wei, S.H. Cui, X. Chen, J.C. Wang, Q. Zhang, Regulating intracellular fate of siRNA by endoplasmic reticulum membrane-decorated hybrid nanoplexes, Nat. Commun. 10 (1) (2019) 2702.
[13] X. Hou, T. Zaks, R. Langer, Y. Dong, Lipid nanoparticles for mRNA delivery, Nat. Rev. Mater. 6 (12) (2021) 1078–1094.
[14] S. Shi, L. Han, T. Gong, Z. Zhang, X. Sun, Systemic delivery of microRNA-34a for cancer stem cell therapy, Angew. Chem. Int. Ed. 52 (14) (2013) 3901–3905.
[15] X. Huang, N. Kong, X. Zhang, Y. Cao, R. Langer, W. Tao, The landscape of mRNA nanomedicine, Nat. Med. 28 (11) (2022) 2273–2287.
[16] M. Bilzer, F. Roggel, A.L. Gerbes, Role of Kupffer cells in host defense and liver disease, Liver Int. 26 (10) (2006) 1175–1186.
[17] W. Ngo, S. Ahmed, C. Blackadar, B. Bussin, Q. Ji, S.M. Mladjenovic, Z. Sepahi, W.C.W. Chan, Why nanoparticles prefer liver macrophage cell uptake in vivo, Adv. Drug Deliv. Rev. 185 (2022) 114238–114249.
[18] Y. Sato, H. Matsui, N. Yamamoto, R. Sato, T. Munakata, M. Kohara, H. Harashima, Highly specific delivery of siRNA to hepatocytes circumvents endothelial cell-mediated lipid nanoparticle-associated toxicity leading to the safe and efficacious decrease in the hepatitis B virus, J. Control. Release 266 (2017) 216–225.
[19] B. Hu, L. Zhong, Y. Weng, L. Peng, Y. Huang, Y. Zhao, X.J. Liang, Therapeutic siRNA: state of the art, Signal Transduct. Tar. 5 (1) (2020) 101.
[20] A.A. D'Souza, P.V. Devarajan, Asialoglycoprotein receptor mediated hepatocyte targeting — strategies and applications, J. Control. Release 203 (2015) 126–139.
[21] A. Sehgal, A. Vaishnaw, K. Fitzgerald, Liver as a target for oligonucleotide therapeutics, J. Hepatol. 59 (6) (2013) 1354–1359.
[22] H. Cui, X. Zhu, S. Li, P. Wang, J. Fang, Liver-targeted delivery of oligonucleotides with N-Acetylgalactosamine conjugation, ACS Omega 6 (25) (2021) 16259–16265.
[23] P. Vervaeke, S.E. Borgos, N.N. Sanders, F. Combes, Regulatory guidelines and preclinical tools to study the biodistribution of RNA therapeutics, Adv. Drug Deliv. Rev. 184 (2022) 114236–114252.
[24] H. Yan, D. Shao, Y.H. Lao, M. Li, H. Hu, K.W. Leong, Engineering cell membrane-based nanotherapeutics to target inflammation, Adv. Sci. 6 (15) (2019) 1900605–1900628.
[25] P. Patel, K.P. Santo, S. Burgess, A. Vishnyakov, A.V. Neimark, Stability of lipid coatings on nanoparticle-decorated surfaces, ACS Nano 14 (12) (2020) 17273–17284.
[26] P. Dash, A.M. Piras, M. Dash, Cell membrane coated nanocarriers - an efficient biomimetic platform for targeted therapy, J. Control. Release 327 (2020) 546–570.
[27] T.P. Prakash, J. Yu, M.T. Migawa, G.A. Kinberger, W.B. Wan, M.E. Østergaard, R.L. Carty, G. Vasquez, A. Low, A. Chappell, K. Schmidt, M. Aghajan, J. Crosby, H.M. Murray, S.L. Booten, J. Hsiao, A. Soriano, T. Machemer, P. Cauntay, S.A. Burel, S.F. Murray, H. Gaus, M.J. Graham, E.E. Swayze, P.P. Seth, Comprehensive structure–activity relationship of triantennary N-acetylgalactosamine conjugated antisense oligonucleotides for targeted delivery to hepatocytes, J. Med. Chem. 59 (6) (2016) 2718–2733.
[28] J.K. Nair, J.L.S. Willoughby, A. Chan, K. Charisse, M.R. Alam, Q. Wang, M. Hoekstra, P. Kandasamy, A.V. Kel'in, S. Milstein, N. Taneja, J. O'Shea, S. Shaikh, L. Zhang, R.J. van der Sluis, M.E. Jung, A. Akinc, R. Hutabarat, S. Kuchimanchi, K. Fitzgerald, T. Zimmermann, T.J.C. van Berkel, M.A. Maier, K.G. Rajeev, M. Manoharan, Multivalent N-acetylgalactosamine-conjugated siRNA localizes in hepatocytes and elicits robust RNAi-mediated gene Silencing, J. Am. Chem. Soc. 136 (49) (2014) 16958–16961.
[29] D. Shao, M. Li, Z. Wang, X. Zheng, Y.-H. Lao, Z. Chang, F. Zhang, M. Lu, J. Yue, H. Hu, H. Yan, L. Chen, W.-f. Dong, K.W. Leong, Bioinspired diselenide-bridged mesoporous silica nanoparticles for dual-responsive protein delivery, Adv. Mater. 30 (29) (2018) 1801198.
[30] D. Shao, F. Zhang, F. Chen, X. Zheng, H. Hu, C. Yang, Z. Tu, Z. Wang, Z. Chang, J. Lu, T. Li, Y. Zhang, L. Chen, K.W. Leong, W.-f. Dong, Biomimetic diselenide-bridged mesoporous organosilica nanoparticles as an X-ray-responsive biodegradable carrier for chemo-immunotherapy, Adv. Mater. 32 (50) (2020) 2004385.
[31] S. Tan, T. Wu, D. Zhang, Z. Zhang, Cell or cell membrane-based drug delivery systems, Theranostics 5 (8) (2015) 863–881.
[32] J. Dong, M. He, J. Li, A. Pessentheiner, C. Wang, J. Zhang, Y. Sun, W.T. Wang, Y. Zhang, J. Liu, S.C. Wang, P.H. Huang, P.L. Gordts, Z.Y. Yuan, S. Tsimikas, J.Y. Shyy, microRNA-483 ameliorates hypercholesterolemia by inhibiting PCSK9 production, JCI Insight 5 (23) (2020) 143812.
[33] C. Chen, Y. Zhou, C. Chen, S. Zhu, X. Yan, Quantification of available ligand density on the surface of targeted liposomal nanomedicines at the single-particle level, ACS Nano 16 (4) (2022) 6886–6897.
[34] A.M. Alkilany, L. Zhu, H. Weller, A. Mews, W.J. Parak, M. Barz, N. Feliu, Ligand density on nanoparticles: a parameter with critical impact on nanomedicine, Adv. Drug Deliv. Rev. 143 (2019) 22–36.
[35] L. Woythe, P. Madhikar, N. Feiner-Gracia, C. Storm, L. Albertazzi, A single–molecule view at nanoparticle targeting selectivity: correlating ligand functionality and cell receptor density, ACS Nano 16 (3) (2022) 3785–3796.
[36] K. Abstiens, M. Gregoritza, A.M. Goepferich, Ligand density and linker length are critical factors for multivalent nanoparticle–receptor interactions, ACS Appl. Mater. Inter. 11 (1) (2019) 1311–1320.
[37] Z. Chen, L. Zhang, Y. Song, J. He, L. Wu, C. Zhao, Y. Xiao, W. Li, B. Cai, H. Cheng, W. Li, Hierarchical targeted hepatocyte mitochondrial multifunctional chitosan nanoparticles for anticancer drug delivery, Biomaterials 52 (2015) 240–250.
[38] W. Poon, Y.-N. Zhang, B. Ouyang, B.R. Kingston, J.L.Y. Wu, S. Wilhelm, W.C.W. Chan, Elimination pathways of nanoparticles, ACS Nano 13 (5) (2019) 5785–5798.
[39] Y. Liu, J. Luo, X. Chen, W. Liu, T. Chen, Cell membrane coating technology: a promising strategy for biomedical applications, Nano-micro Lett 11 (1) (2019) 100.
[40] C.D. Byrne, G. Targher, NAFLD: a multisystem disease, J. Hepatol. 62 (1, Supplement) (2015) S47–S64.
[41] G. Bisaccia, F. Ricci, E. Melchiorre, C. Tana, G. Renda, M.Y. Khanji, A. Fedorowski, R. De Caterina, S. Gallina, Cardiovascular morbidity and mortality related to non-alcoholic fatty liver disease: a systematic review and meta-analysis of prospective studies, Eur. Heart J. 42 (Supplement_1) (2021) ehab724.2462.
[42] D. Steinberg, J.L. Witztum, Inhibition of PCSK9: a powerful weapon for achieving ideal LDL cholesterol levels, Proc. Natl. Acad. Sci. U. S. A. 106 (24) (2009) 9546–9547.
[43] R.M. Rodrigues, Y. Guan, B. Gao, Targeting adipose tissue to tackle NASH: SPARCL1 as an emerging player, J. Clin. Invest. 131 (20) (2021).
[44] G.C. Hugenholtz, P.G. Northup, R.J. Porte, T. Lisman, Is there a rationale for treatment of chronic liver disease with antithrombotic therapy? Blood Rev 29 (2) (2015) 127–136.

[45] M.W. Stavinoha, R.D. Soloway, Current therapy of chronic liver disease, Drugs 39 (6) (1990) 814–840.
[46] A. Paul, A. Muralidharan, A. Biswas, B.V. Kamath, A. Joseph, A.T. Alex, siRNA therapeutics and its challenges: recent advances in effective delivery for cancer therapy, OpenNano 7 (2022) 100063.
[47] J.L.S. Willoughby, A. Chan, A. Sehgal, J.S. Butler, J.K. Nair, T. Racie, S. Shulga-Morskaya, T. Nguyen, K. Qian, K. Yucius, K. Charisse, T.J.C. van Berkel, M. Manoharan, K.G. Rajeev, M.A. Maier, V. Jadhav, T.S. Zimmermann, Evaluation of GalNAc-siRNA conjugate activity in pre-clinical animal models with reduced asialoglycoprotein receptor expression, Mol. Ther. 26 (1) (2018) 105–114.
[48] Z. Zeng, K. Pu, Improving cancer immunotherapy by cell membrane-camouflaged nanoparticles, Adv. Funct. Mater. 30 (43) (2020) 2004397.
[49] M. Izci, C. Maksoudian, B.B. Manshian, S.J. Soenen, The use of alternative strategies for enhanced nanoparticle delivery to solid tumors, Chem. Rev. 121 (3) (2021) 1746–1803.
[50] H. Wang, R. Wang, K. Cai, H. He, Y. Liu, J. Yen, Z. Wang, M. Xu, Y. Sun, X. Zhou, Q. Yin, L. Tang, I.T. Dobrucki, L.W. Dobrucki, E.J. Chaney, S.A. Boppart, T.M. Fan, S. Lezmi, X. Chen, L. Yin, J. Cheng, Selective in vivo metabolic cell-labeling-mediated cancer targeting, Nat. Chem. Biol. 13 (4) (2017) 415–424.
[51] Q. Zhang, W. Wei, P. Wang, L. Zuo, F. Li, J. Xu, X. Xi, X. Gao, G. Ma, H.-y. Xie, Biomimetic magnetosomes as versatile artificial antigen-presenting cells to potentiate T-cell-based anticancer therapy, ACS Nano 11 (11) (2017) 10724–10732.
[52] D.E. Sastre, L.G.M. Basso, B. Trastoy, J.O. Cifuente, X. Contreras, F. Gueiros–Filho, D. de Mendoza, M.V.A.S. Navarro, M.E. Guerin, Membrane fluidity adjusts the insertion of the transacylase PlsX to regulate phospholipid biosynthesis in Gram-positive bacteria, J. Biol. Chem. 295 (7) (2020) 2136–2147.
[53] S. Yonezawa, H. Koide, T. Asai, Recent advances in siRNA delivery mediated by lipid-based nanoparticles, Adv. Drug Deliv. Rev. 154-155 (2020) 64–78.
[54] Y.-N. Zhang, W. Poon, A.J. Tavares, I.D. McGilvray, W.C.W. Chan, Nanoparticle–liver interactions: cellular uptake and hepatobiliary elimination, J. Control. Release 240 (2016) 332–348.
[55] S. Dow, Liposome-nucleic acid immunotherapeutics, Expert Opin. Drug Deliv. 5 (1) (2008) 11–24.
[56] E. Ren, C. Liu, P. Lv, J. Wang, G. Liu, Genetically engineered cellular membrane vesicles as tailorable shells for therapeutics, Adv. Sci. 8 (21) (2021) 2100460.
[57] J. Lopes, D. Lopes, M. Pereira-Silva, D. Peixoto, F. Veiga, M.R. Hamblin, J. Conde, C. Corbo, E.N. Zare, M. Ashrafizadeh, F.R. Tay, C. Chen, R.F. Donnelly, X. Wang, P. Makvandi, A.C. Paiva-Santos, Macrophage cell membrane-cloaked nanoplatforms for biomedical applications, Small Methods 6 (8) (2022) 2200289.
[58] V. Chugh, K. Vijaya Krishna, A. Pandit, Cell membrane-coated mimics: a methodological approach for fabrication, characterization for therapeutic applications, and challenges for clinical translation, ACS Nano 15 (11) (2021) 17080–17123.
[59] B. Hu, B. Li, K. Li, Y. Liu, C. Li, L. Zheng, M. Zhang, T. Yang, S. Guo, X. Dong, T. Zhang, Q. Liu, A. Hussain, Y. Weng, L. Peng, Y. Zhao, X.-J. Liang, Y. Huang, Thermostable ionizable lipid-like nanoparticle (iLAND) for RNAi treatment of hyperlipidemia, Sci. Adv. 8 (7) (2022) eabm1418.